Article

Cell Reports

OTUB1 Is a Key Regulator of RIG-I-Dependent Immune Signaling and Is Targeted for Proteasomal Degradation by Influenza A NS1

Graphical Abstract

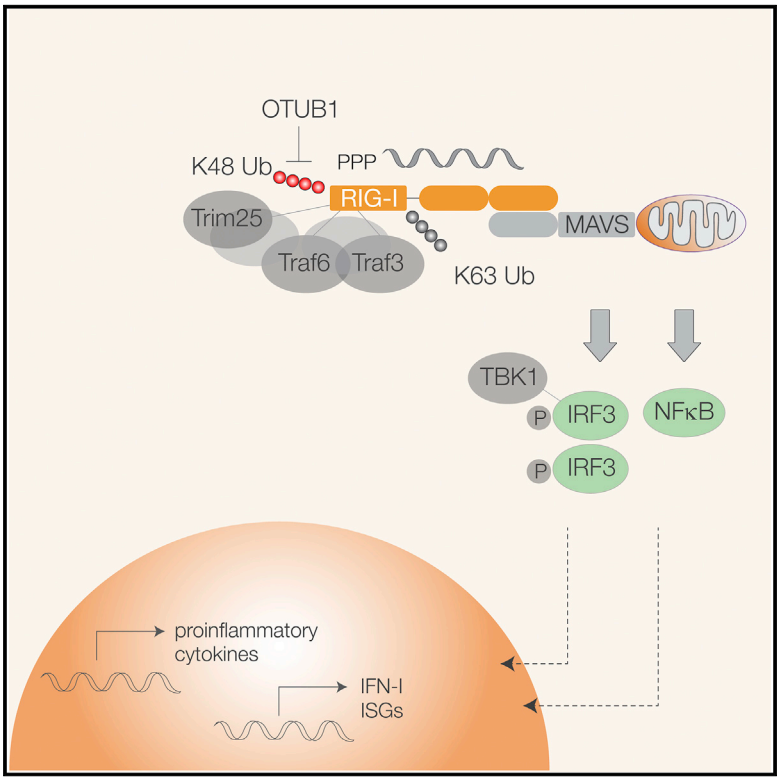

Authors

Akhee Sabiha Jahan, Elise Biquand, Raquel Muñoz-Moreno, ..., Adolfo García-Sastre, Caroline Demeret, Sumana Sanyal

Correspondence

sanyal@hku.hk

In Brief

Jahan et al. describe the role of Otub1, a deubiquitylase that is induced during virus infection in an interferon-dependent manner to regulate optimal signaling via the RIG-I pathway. Influenza A virus NS1 is able to bind and degrade newly synthesized Otub1 as a means to evade the innate immune response.

Highlights

- OTUB1 is induced during IAV infection in an IFN-I-dependent manner
- OTUB1 regulates the RIG-I complex via its enzymatic and E2-repressive activities
- Optimal K63 versus K48 polyubiquitin chain concentrations determine RIG-I activation
- Influenza NS1 targets OTUB1 for proteasomal degradation

Jahan et al., 2020, Cell Reports *30*, 1570–1584
February 4, 2020
https://doi.org/10.1016/j.celrep.2020.01.015

CellPress

OPEN ACCESS
CellPress

Cell Reports
Article

OTUB1 Is a Key Regulator of RIG-I-Dependent Immune Signaling and Is Targeted for Proteasomal Degradation by Influenza A NS1

Akhee Sabiha Jahan,[1,2] Elise Biquand,[5,10] Raquel Muñoz-Moreno,[6,7] Agathe Le Quang,[1,2] Chris Ka-Pun Mok,[1,2] Ho Him Wong,[1,2] Qi Wen Teo,[1,2] Sophie A. Valkenburg,[1,2] Alex W.H. Chin,[2] Leo Lit Man Poon,[2] Artejan te Velthuis,[4] Adolfo García-Sastre,[6,7,8,9] Caroline Demeret,[5] and Sumana Sanyal[1,2,3,11,12,*]

[1]HKU-Pasteur Research Pole, University of Hong Kong, Hong Kong
[2]School of Public Health, LKS Faculty of Medicine, University of Hong Kong, Hong Kong
[3]School of Biomedical Sciences, LKS Faculty of Medicine, University of Hong Kong, Hong Kong
[4]Division of Virology, Department of Pathology, University of Cambridge, Addenbrooke's Hospital, Cambridge, UK
[5]Molecular Genetics of RNA Viruses, CNRS UMR 3569, Université de Paris, Institut Pasteur, Paris, France
[6]Department of Microbiology, Icahn School of Medicine at Mount Sinai, New York, NY 10029, USA
[7]Global Health and Emerging Pathogens Institute, Icahn School of Medicine at Mount Sinai, New York, NY 10029 USA
[8]Division of Infectious Diseases, Department of Medicine, Icahn School of Medicine at Mount Sinai, New York, NY 10029 USA
[9]The Tisch Cancer Institute, Icahn School of Medicine at Mount Sinai, New York, NY 10029 USA
[10]Present address: Oncology Division, CHU de Québec-Université Laval Research Center; Cancer Research Center; and Department of Molecular Biology, Medical Biochemistry and Pathology, Université Laval, Québec, Canada
[11]Present address: Sir William Dunn School of Pathology, South Parks Road, Oxford, England OX1 3RE, UK
[12]Lead Contact
*Correspondence: sanyal@hku.hk
https://doi.org/10.1016/j.celrep.2020.01.015

SUMMARY

Deubiquitylases (DUBs) regulate critical signaling pathways at the intersection of host immunity and viral pathogenesis. Although RIG-I activation is heavily dependent on ubiquitylation, systematic analyses of DUBs that regulate this pathway have not been performed. Using a ubiquitin C-terminal electrophile, we profile DUBs that function during influenza A virus (IAV) infection and isolate OTUB1 as a key regulator of RIG-I-dependent antiviral responses. Upon infection, OTUB1 relocalizes from the nucleus to mitochondrial membranes together with RIG-I, viral PB2, and NS1. Its expression depends on competing effects of interferon stimulation and IAV-triggered degradation. OTUB1 activates RIG-I via a dual mechanism of K48 polyubiquitin hydrolysis and formation of an E2-repressive complex with UBCH5c. We reconstitute this mechanism in a cell-free system comprising [^{35}S]IRF3, purified RIG-I, mitochondrial membranes, and cytosol expressing OTUB1 variants. A range of IAV NS1 proteins trigger proteasomal degradation of OTUB1, antagonizing the RIG-I signaling cascade and antiviral responses.

INTRODUCTION

Innate immunity against viral infections is triggered when germline-encoded pattern recognition receptors (PRRs) sense the presence of viral nucleic acids or other virus-specific components. The retinoic acid-inducible gene I (RIG-I)-like receptor (RLR) family constitutes one such group of cytosolic PRRs that is important in sensing viral RNA. Current evidence supports the activity of three members of the RLR family: RIG-I, melanoma differentiation-associated gene 5 (MDA-5), and laboratory of genetics and physiology 2 (LGP2). RIG-I and MDA-5 detect a wide range of RNA viruses and share several structural similarities but often display differences in a cell-type- and virus-strain-specific manner (Jiang et al., 2012; Rehwinkel et al., 2010).

Many viral sensing and immune response mechanisms derive from functional and structural studies of RIG-I (Yoneyama and Fujita, 2008). Upon binding to double-stranded RNA (dsRNA), RIG-I transforms from an auto-repressed to an open conformation (Kowalinski et al., 2011); this facilitates its tetramerization and K63-linked ubiquitylation by either TRIM25 or RIPLET (Cadena et al., 2019; Gack et al., 2007). RIG-I tetramers translocate to mitochondrial membranes (Liu et al., 2012), where they interact with mitochondrial antiviral signaling (MAVS) protein via their respective CARD domains. The resulting complex recruits downstream effector molecules (Gack, 2014; Pauli et al., 2014; Zeng et al., 2010) and activates IRF3, IRF7, and nuclear factor κB (NF-κB) to produce interferon-I (IFN-I), ultimately creating an antiviral state.

Ubiquitylation, historically described for removal of misfolded proteins, has emerged as a critical regulator for fine-tuning signal transduction processes, and the RIG-I pathway is no exception. The mode of RIG-I ubiquitylation and its implications on signaling have been subjects of intense research in the past few years. K63 ubiquitin chains, either in their free or conjugated forms, are critical for RIG-I signal transduction. Until recently, K63 ubiquitylation was thought to be catalyzed interchangeably by TRIM25 and RIPLET; however, recent studies have indicated that RIG-I activation is fundamentally dependent on RIPLET (Cadena et al., 2019).

All ubiquitin-dependent processes are accompanied by an additional layer of regulation by deubiquitylases (DUBs) (Komander et al., 2009). DUBs are an important class of enzymes, and many have been implicated in human diseases (Reyes-Turcu et al., 2009). In immune signaling cascades, A20 (Catrysse et al., 2014), CYLD (Trompouki et al., 2003), OTULIN, USP12, and Cezanne function as regulators in NF-κB and T cell signaling (Düwel et al., 2009; Jahan et al., 2016). Given the essential role of ubiquitylation both upstream and downstream in the multi-step RIG-I signal cascade, it is very likely that DUBs have key regulatory functions in this pathway. A few have been implicated previously. USP21 is able to remove K63 chains from RIG-I (Fan et al., 2014), USP4 hydrolyzes K48 chains from transiently transfected RIG-I (Wang et al., 2013), and OTUD1 facilitated degradation of MAVS by stabilizing an E3-ligase (Zhang et al., 2018b).

In this study, we applied activity-based profiling (Ovaa et al., 2004) to uncover DUBs that function during influenza A virus (IAV) infection and identified OTUB1 as a critical regulator of RIG-I activation. We established that OTUB1 is key for optimal RIG-I signaling and functions via a coordinated mechanism of hydrolyzing K48 chains and forming an E2-repressive complex. Knockout of OTUB1 resulted in loss of oligomeric RIG-I, disassembly of the signaling complex, and failure of NF-κB and interferon regulatory factor (IRF) activation in IAV-infected cells. We recapitulated this phenomenon in a reconstituted cell-free system to define the underlying mechanism of OTUB1 function in this pathway. Hydrolysis of K48 polyubiquitin chains and sequestration of UBCH5c by OTUB1 were prerequisites for K63 polyubiquitylation of RIG-I. Catalytically inactive OTUB1 displayed partial loss of IRF3 dimerization; on the other hand, mutants that did not form the E2-repressive complex or failed to relocalize to mitochondrial membranes abolished IRF3 activation. This phenomenon was antagonized by IAV NS1, which triggered proteasomal degradation of newly synthesized OTUB1. Our results therefore provide fundamental insights into the mechanism of maintaining fidelity and optimal magnitude in the RIG-I signal transduction cascade and highlight the complex interplay between immune responses and viral antagonism.

RESULTS

Identification of Host DUBs Activated upon IAV Infection

Total cellular ubiquitylation profiles are often altered in IAV-infected cells, depending on the severity of pathogenesis. To establish whether this occurs in a strain-specific manner, we detected bulk ubiquitylation in IAV-infected A549 cells expressing wild-type ubiquitin. K48-, K63-, and M1-linked ubiquitylated proteins from mock- and virus-infected cells were isolated by linkage-specific tandem ubiquitin-binding entities (TUBEs). Although K48-linked ubiquitylation was consistently lower in infected cells, K63-ubiquitylated species were more pronounced in IAV-infected cells compared with mock-infected cells. No significant changes were detectable in (M1) linear chains between the different IAV strains; however, they were elevated in infected cells compared with mock-infected cells. Bulk profiles indicated distinct differences that exist in the dynamics of ubiquitylation upon infection by different flu viruses (Figure 1A).

To isolate DUBs from IAV-infected cells, we followed an experimental setup as illustrated (Figure 1B; Jahan et al., 2016; Zhang et al., 2018a) and applied previously to isolate cellular DUBs (Jahan et al., 2016; Kwasna et al., 2018). Mock- and H1N1 pandemic IAV-infected primary lung epithelial cells or A549 cells were permeabilized using perfringolysin O (Sanyal et al., 2012, 2013), and activated DUBs were isolated with ubiquitin-vinylmethylester (Ub-vme) carrying a TAMRA or hemagglutinin (HA) tag. Ub-vme-reactive materials from control and infected cells were resolved by SDS-PAGE and visualized by fluorescence scanning (Figure 1C) or enriched on anti-HA beads first and detected by silver staining (Figure 1D). Potential candidates were identified by trypsin digestion, mass spectrometry, and spectral counting of peptides on immunoprecipitated material (Table S1).

We validated the mass spectrometry (MS) hits in lysates prepared from mock-infected, IAV-infected, or IFN-I-treated samples by immunoblotting and detected a shift in molecular weight in proteins that reacted with Ub-vme (Figure 1E). Among identified candidates were known regulators of IFN signaling such as Usp25 (Lin et al., 2015), Usp15 (Pauli et al., 2014), and DUBA, which displayed reduced expression in H1N1-infected cells and high Ub-vme reactivity in IFN-I-treated samples, in agreement with a previous report (Kayagaki et al., 2007).

OTUB1 Expression Is Induced by IFN-I and Degraded by IAV

OTUB1 is a member of the ovarian tumor domain containing a superfamily of proteases. It has a catalytic cysteine (C91), several phosphorylation sites (phosphorylation on S16 can determine cytosolic versus nuclear localization of OTUB1; Herhaus et al., 2015), and hydrolyzes K48 ubiquitin chains (Edelmann et al., 2009; Juang et al., 2012; Figure 2A). It is also able to inhibit ubiquitylation via its non-canonical activity of sequestering E2 enzymes (Juang et al., 2012).

OTUB1 expression levels increased as a function of time and peaked ~12 h after infection in multicycle IAV infections (Figure 2B). This was followed by its degradation at later time points, a phenomenon recapitulated in both A549 and primary lung epithelial cells, with all IAV strains (Figures 2B and 2C). To uncouple its induction from degradation, we performed infections in Vero cells deficient in IFN production, where IAV-dependent degradation of OTUB1 was more apparent (Figure 2D). Vero cells treated with exogenous IFN-β displayed a significant increase in the expression of OTUB1, but not its degradation, suggesting that the latter phenomenon was very likely virus mediated. Stimulation with other ligands (lipopolysaccharide [LPS], poly(I:C)) did not have a significant effect on OTUB1 protein levels in Vero cells deficient in transcriptional induction of IFN-I (Figure 2D).

To further verify IFN-I-dependent induction of OTUB1, we treated IFN receptor-proficient ($IFNAR^{+/+}$) and deficient ($IFNAR^{-/-}$) cells with exogenous IFN-I. Induction of OTUB1 was specific to $IFNAR^{+/+}$ cells (Figure 2E). To exclude NF-κB-induced OTUB1 expression, we treated cells with Jsh-23, which

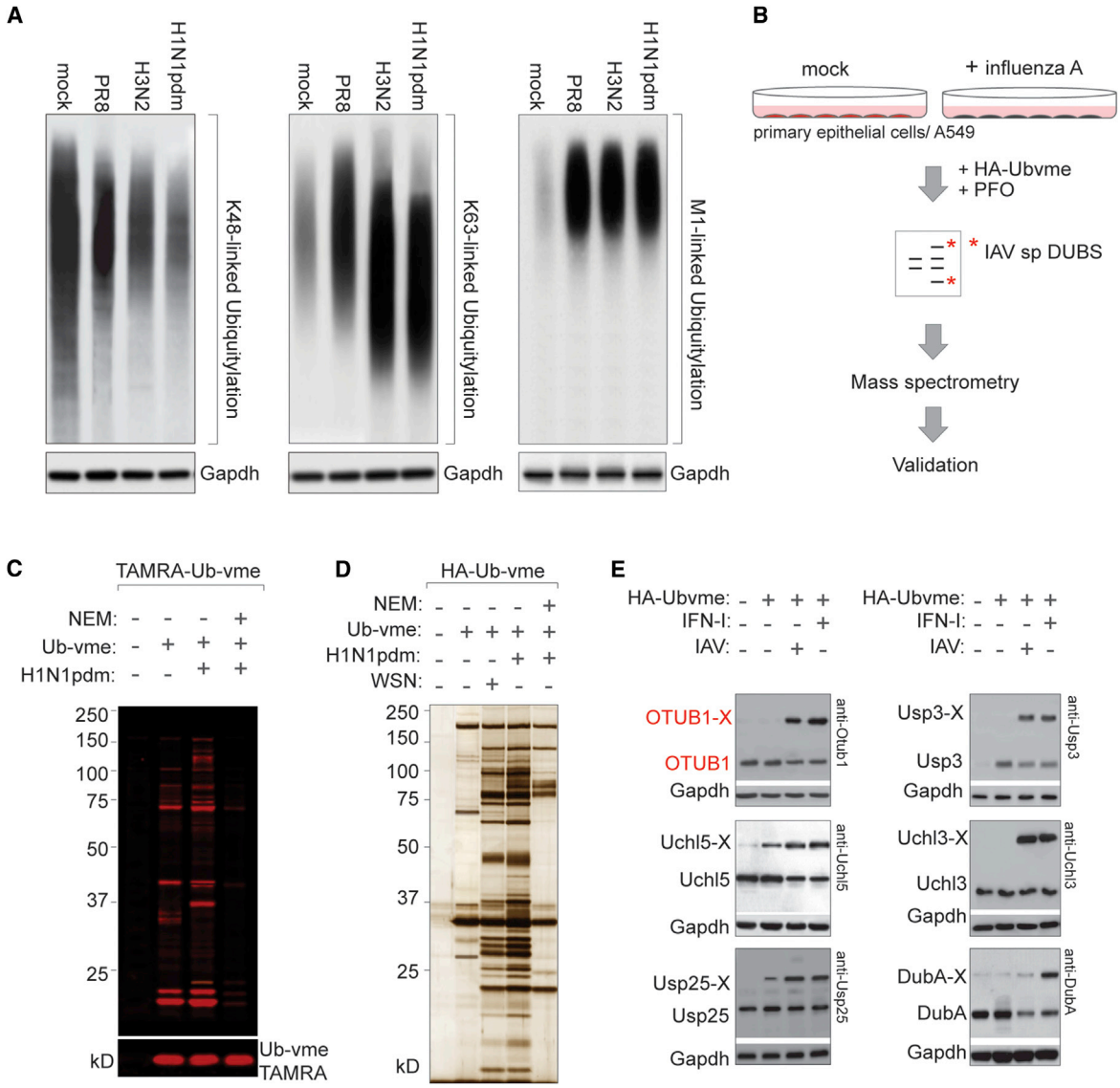

Figure 1. Identification of DUBs Activated upon IAV Infection

(A) Linkage-specific ubiquitylation profiles isolated from mock- and IAV-infected samples. A549 cells expressing WT ubiquitin were infected with different strains of IAV (MOI 1.0, 10 h): A/PR/8/34, A/H1N1pdm09, and *A/Oklahoma/309*/06 (H3N2). Ubiquitylated proteins were isolated on linkage-specific tandem ubiquitin-binding entities (TUBEs), resolved by SDS-PAGE, and detected by anti-ubiquitin antibodies.

(B) Schematic of isolation of DUBs activated upon IAV infection.

(C and D) 5 μM TAMRA-tagged (C) and 10 μM HA-tagged (D), Ub-vme-treated, mock- and IAV-infected primary epithelial cells. Ag-stained profiling of large-scale immunoprecipitation (IP) of Ubvme-modified DUBs from mock- and IAV-infected cells was performed with 15 × 10^6 cells/condition. Entire lanes were sliced into 2-mm sections and subjected to MS/MS on an LTQ Orbitrap instrument for protein identification.

(E) Validation of identified proteins and their reactivity toward Ub-vme (5 μM) was performed in lysates prepared from IAV-infected (MOI 1.0, 10 h) or IFN-treated (IFN-β, 200 IU/mL, 5 h) samples and verified by immunoblotting.

blocks translocation of the p65 subunit from the cytosol to the nucleus and subsequent expression of downstream genes. Jsh-23 treatment restricted p65 distribution to cytosol fractions in both H1N1-infected and IFN-I-treated cells (Figure 2F, top panel). The expression profiles of OTUB1 however, remained unaffected in lysates collected at the indicated time intervals regardless of Jsh-23 treatment, suggesting that its induction occurs independent of NF-κB activation (Figure 2E, bottom panel).

OTUB1 Is Redistributed to Mitochondrial Membranes and Co-segregates with RIG-I during Infection

To determine with what OTUB1 associates in IAV-infected cells, we measured its localization by confocal imaging and neighboring partners by proximity-based labeling. In uninfected cells, OTUB1 resided largely in the nucleus; upon infection, it relocalized from the nucleus to the cytosol and mitochondrial membranes. A significant fraction colocalized with TOMM20, a

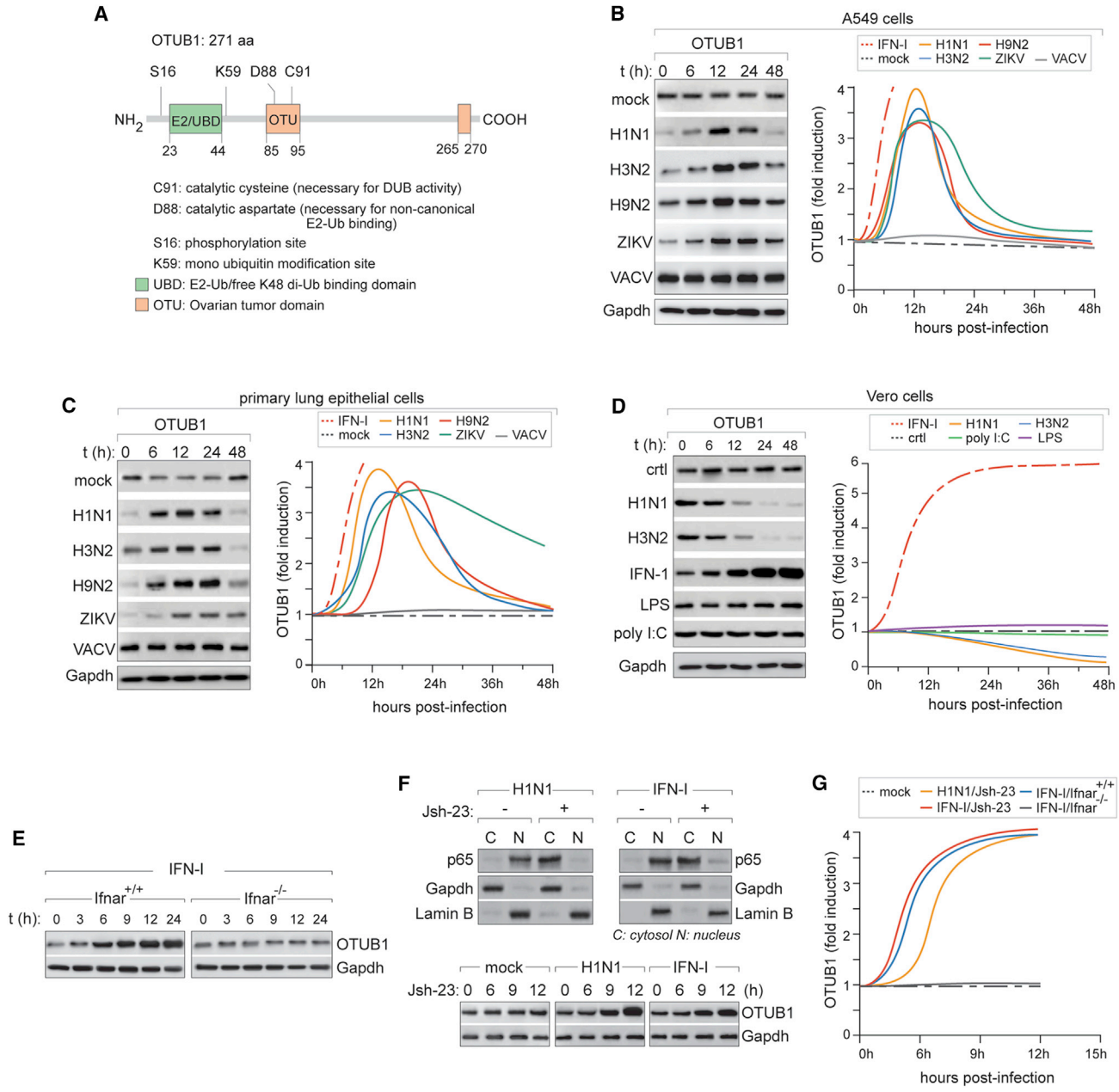

Figure 2. OTUB1 Is IFN Inducible and Degraded upon Influenza Infection

(A) Schematic of the domain architecture of OTUB1, showing its catalytic site, OTU domain, and ubiquitin binding domain (UBD)/E2-binding region, with specific mutations in residues that were used in this study.

(B) Steady-state levels of OTUB1 in A549 cells infected with different strains of IAV (MOI 0.1) for the indicated time intervals. Zika virus (ZIKV) and vaccinia virus (VACV) were used as controls (left panel). Lysates collected at the indicated time points after infection were immunoblotted with antibodies to endogenous OTUB1. Densitometric analyses of protein expression were performed with ImageJ and normalized to 0 h. Curve fitting was performed with data from at least three independent experiments (right panel).

(C) Steady-state levels of OTUB1 in primary lung epithelial cells stimulated with different viruses and assessed as in (B). Curve fits were generated with data from at least 3 independent experiments.

(D) Steady-state levels of OTUB1 in Vero cells stimulated with either IAV or ligands alone; LPS was used to stimulate TLR4 and poly(I:C) for RIG-I. Samples were process as in (B) and (C).

(E) WT and IFNAR$^{-/-}$ HAP1 cells were treated with IFN-β (250 IU/mL) for the indicated time intervals. Lysates prepared from samples at each time point were immunoblotted for expression of OTUB1.

(legend continued on next page)

mitochondrial marker, specifically in infected cells but not in mock-infected cells (Figure 3A). Phosphorylation-defective mutants of OTUB1 (Herhaus et al., 2015), S16A (phospho-deficient) and S16E (phosphomimetic), were enriched in the cytosol and nucleus, respectively, whereas C91S, the catalytically dead variant, and the D88A mutant, defective in binding E2 enzymes, displayed a similar intracellular distribution as that of the wild type (Figure S1).

To identify its potential interactors in mock- and IAV-infected cells, we first expressed a BioID-OTUB1 construct in the wild-type (WT) or OTUB1$^{-/-}$ background (Figure 3B) and cultured cells in biotin-supplemented medium. Biotinylated proteins were captured by streptavidin beads, resolved by SDS-PAGE, and identified by LC-MS/MS (Figures 3C and 3D). Identified candidates were sorted by functional enrichment of pathways using Ingenuity Pathway Analysis. The isolated candidates indicated that OTUB1 preferentially associated with components of the RIG-I signaling pathway in IAV-infected samples compared with mock-infected samples, in which it primarily associated with RNA helicases in the nucleus. Among the viral factors, we identified PB2, as reported previously (Biquand et al., 2017), and NS1. To confirm the MS data, we separated lysates from mock- and IAV-infected cells by sedimentation on glycerol gradients, where OTUB1 co-migrated with high-molecular-weight RIG-I oligomers in IAV-infected but not in mock-infected cells (Figure 3E). Interestingly, although IAV NS1 was distributed uniformly, PB2 displayed two peaks, one coinciding with that of oligomeric RIG-I, which presumably corresponds to the mitochondrial fraction of PB2. These data suggest that OTUB1 is recruited to mitochondrial membranes along with active RIG-I tetramers. As further validation, we isolated mitochondria using a commercially available isolation kit, verified by measuring enrichment of the respiratory chain components (total OXPHOS complexes) (Figure 3F). In IAV-infected cells but not mock-treated cells, myc-tagged RIG-I partitioned with the mitochondrion-enriched pellet (P) fractions. OTUB1 specifically co-precipitated with this fraction of RIG-I, further confirming their co-segregation at the mitochondrial membranes (Figure 3G).

OTUB1 Deletion Results in Defective NF-κB and IRF Responses during RNA Virus Infection

To determine the functional effect of OTUB1 on RIG-I signaling, we generated OTUB1$^{-/-}$ A549 cells. Single clones selected after serial dilution were expanded to verify deletion by immunoblotting. WT OTUB1 was then reconstituted back into the deletion background (rOTUB1) (Figure 4A, left panel). In parallel, we generated OTUB1$^{-/-}$ A549 cells expressing a dual reporter for IRF and NF-κB activities (A549^{dual}), measured via luciferase and secreted alkaline phosphatase, respectively. OTUB1 was deleted in either the WT or a RIG-I$^{-/-}$ background in these reporter cells (Figure 4A, right panel).

Infection by RNA viruses and subsequent RIG-I signaling is accompanied by activation of NF-κB and IRF3, which can be detected by phosphorylation of the p65 subunit of NF-κB and dimerization of IRF3. To monitor their activities in OTUB1$^{-/-}$ and rOTUB1 cells, we measured the appearance of IRF3 dimers and phosphorylated p65. In both instances, OTUB1 deficiency resulted in loss of these activities, but they were rescued in rOTUB1 cells (Figures 4B and 4C). Defective IRF3 activity was also verified in primary lung epithelial cells upon small interfering RNA (siRNA)-mediated depletion of OTUB1 (Figure S2D).

To establish how universal this effect was, we infected A549^{dual} cells (WT, OTUB1$^{-/-}$, RIG I$^{-/-}$, or OTUB1$^{-/-}$RIG I$^{-/-}$ double knockout) with different strains of IAV, Zika, encephalomyocarditis virus (EMCV), and a DNA virus (Vaccinia) in the sample set. Supernatants collected at different time intervals were quantitated for NF-κB activity by measuring the absorbance of secreted alkaline phosphatase at 620 nm. For all strains of influenza as well as for poly(I:C) treatment, a significant reduction in NF-κB activity was recorded in OTUB1$^{-/-}$ cells, comparable with RIG-I$^{-/-}$ cells. No additive effect was noted in the double knockout cells, suggesting that they most likely function in the same pathway (Figures 4D and S2A). As with NF-κB activation, OTUB1$^{-/-}$ cells displayed significantly diminished IRF activity upon infection with different strains of influenza as well as with poly(I:C) (Figures 4E and S2A). On the other hand, OTUB1 deficiency did not have any effect on LPS-dependent activation of NF-κB or IRF (Figure S2B). Collectively, our results indicate that OTUB1 deficiency inhibits NF-κB and IRF activities, suggesting that it acts upstream of these transcription factors in the RIG-I signaling cascade. OTUB1 deficiency had a partial effect on IRF activity with Zika virus too, which is sensed by both RIG-I and MDA5 (Figure 4F); however, no effect was detected with EMCV, which predominantly triggers MDA5 (Figure 4G). Neither did it have any effect on STING activation with cyclic 2′3′-cGAMP (Figure 4H, I) or with Vaccinia infection because the predominant virus sensing and immune activation to DNA viruses is mediated by cGas/STING (Figure S2C).

The RIG-I Signaling Complex Disassembles in the Absence of OTUB1

In uninfected cells, RIG-I remains folded with its CARD domains in an auto-repressed inactive conformation. Upon infection, viral dsRNA binding exposes the CARD domains, which interact with K63 polyubiquitin chains and a multitude of effector molecules for optimal signal transduction in the RIG-I-MAVS-TBK1-IRF3 axis (Figure 5A). To determine whether formation of the RIG-I signaling complex requires OTUB1, we transduced myc-RIG-I into RIG-I$^{-/-}$ A549 cells carrying a deletion of OTUB1 or expressing a WT copy and infected with H1N1(pdm). IFN-α production was completely lost in OTUB1$^{-/-}$ cells and rescued when reconstituted with WT OTUB1 but also partially in cells stably expressing myc-RIG-I, suggesting that compensatory mechanisms might be activated in these cells (Figure S3B). Most of the signaling molecules displayed enhanced expression in lysates from IAV-infected cells compared with mock-infected cells

(F) A549 cells were left untreated or treated with 10 μM NF-κB inhibitor Jsh-23 and infected with H1N1(pdm) at MOI 0.1 (left panel) or 100 IU/mL IFN-β for 12 h (right panel).
(G) Densitometric analyses of protein expression in (E) and (F) were performed with ImageJ and normalized to 0 h. Curve fits were generated with data from at least three independent experiments.

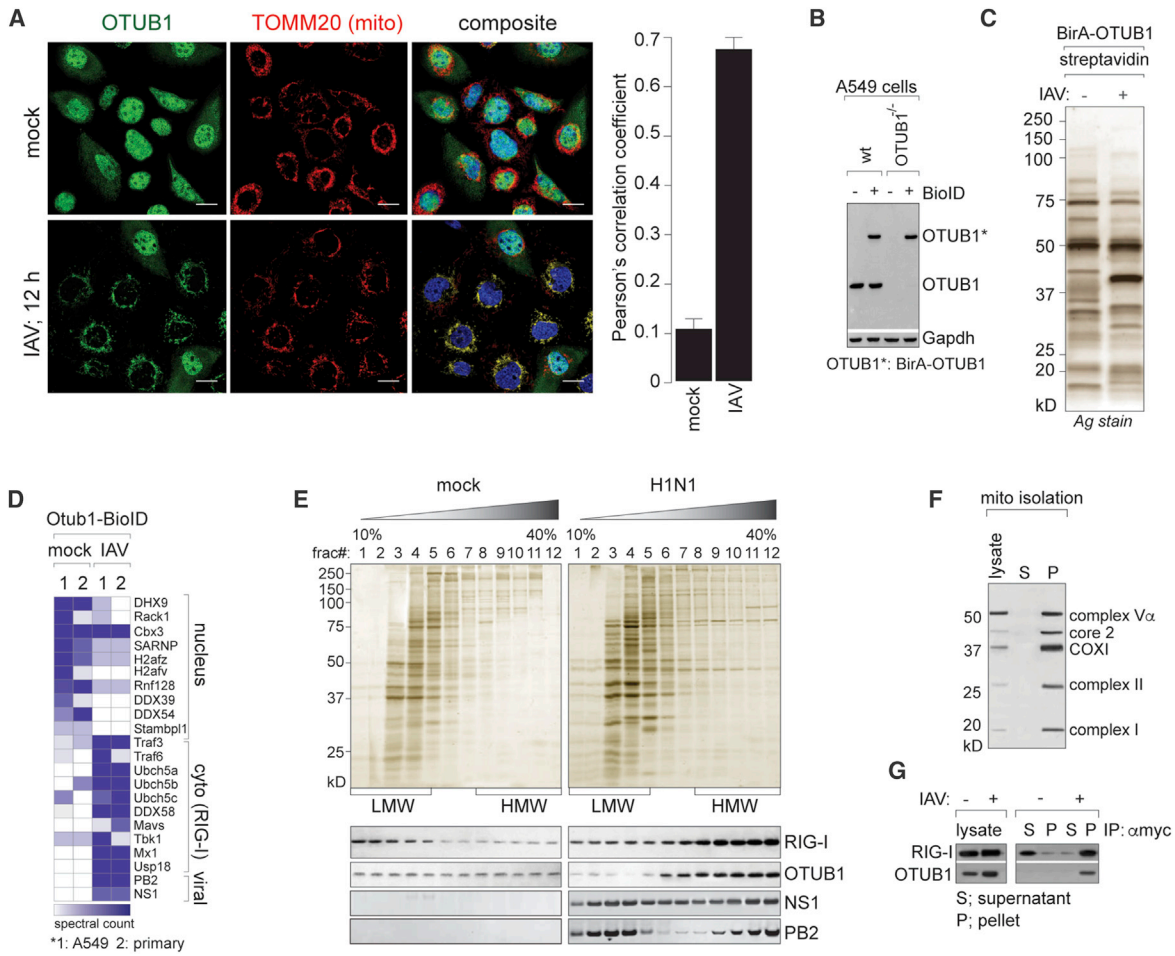

Figure 3. OTUB1 Is Distributed to the Cytosol and Mitochondrial Membranes upon Infection

(A) OTUB1 distribution (green) and TOMM20 (red) were visualized in mock-treated and IAV-infected samples (MOI 1.0, 8 h) using confocal imaging. Scale bars, 10 μm. Images are representative of more than 3 independent experiments. Pearson's correlation coefficient was determined to quantitate colocalization of OTUB1 and TOMM20 (right panel).

(B) Stable expression of the BioID-OTUB1 construct in either WT or OTUB1$^{-/-}$ A549 cells was verified by immunoblotting.

(C) Ag-stained gel of immunoprecipitated material, captured on streptavidin beads, from mock- and IAV-infected A549 cells stably transduced with BioID-OTUB1. 2-mm slices from entire lanes were processed and injected into a Lumos Orbitrap mass spectrometer for peptide identification.

(D) Spectral counts determined for candidates identified by MS were rank ordered with a threshold of 5-fold difference between mock and infected samples. Significant hits were categorized into Gene Ontology (GO) terms using Ingenuity Pathway Analysis. Two independent biological replicates from different cell types (A549 and primary lung epithelial cells) were performed for MS analyses.

(E) Lysates prepared from mock- and IAV-infected cells were separated by velocity sedimentation on glycerol gradients (10%–40%); fractions collected from the top were resolved by SDS-PAGE and detected by Ag staining (top panel). The migration characteristics of RIG-I, OTUB1, and IAV proteins NS1 and PB2 from mock- and IAV-infected cells were determined by immunoblotting. HMW (high-molecular-weight) species and LMW (low-molecular-weight) species were calibrated by internal markers.

(F) A549 cells were ruptured using a Dounce homogenizer, followed by mitochondrial isolation using the manufacturer's protocol. Enrichment of mitochondria was verified on 2 μg of total protein via western blotting with the MitoProfile Total OXPHOS detection kit.

(G) Mitochondrial fractions were isolated from mock- and H1N1-infected A549 cells expressing myc-RIG-I, as described in (F). Expression of total RIG-I and OTUB1 was measured in lysates. IP of RIG-I was performed with anti-myc from the supernatant (S) and mitochondrion-enriched pellet (P) fractions. Co-precipitation of OTUB1 in the corresponding fractions was measured by immunoblotting.

(Figure 5B). Although all of them co-precipitated with myc-RIG-I from cells expressing OTUB1 (either WT or reconstituted cells), this failed in the absence of OTUB1 (Figure 5C, left panel). K63 polyubiquitin chains could also be captured with RIG-I in WT cells or those reconstituted with OTUB1 but failed to co-purify in OTUB1$^{-/-}$ cells. We further investigated this complex by sedimentation over glycerol gradients. Lysates from IAV-infected WT or OTUB1$^{-/-}$ cells were separated by sedimentation over 10%–40% linear glycerol gradients. The collected fractions were immunoblotted for RIG-I and associated partners. Most of the signaling components co-migrated with high-molecular-weight RIG-I in WT cells but not in OTUB1$^{-/-}$ cells (Figure 5D).

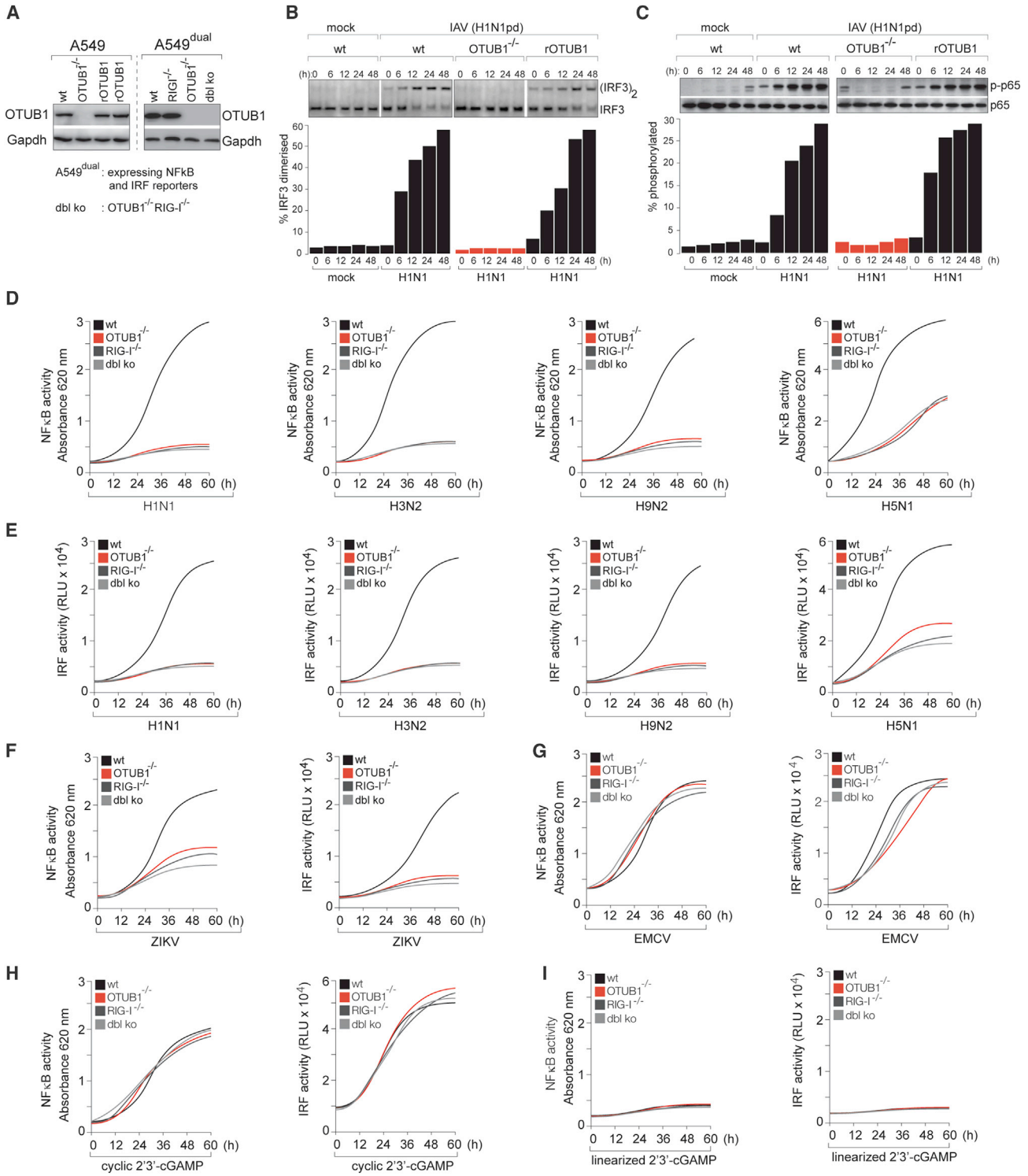

Figure 4. OTUB1 Deficiency Blocks NF-κB and IRF Activation

(A) Clonal isolates of OTUB1 knockout generated by CRISPR/Cas9 and those reconstituted with WT OTUB1 in A549 cells; lysates were used for immunoblotting (anti-OTUB1) to verify deletion and expression (left panel). Single clones of OTUB1-deleted A549 cells expressing a dual reporter for NF-κB and IRF activities were generated that were either WT or deleted in RIG-I (right panel).

(B) Activation of IRF3 was measured in mock- and IAV-infected cells (either WT, OTUB1$^{-/-}$, or reconstituted with WT OTUB1 [(rOTUB1]). IRF3 dimers were resolved and detected by native PAGE.

(legend continued on next page)

This effect also extended to MAVS oligomerization. Although its expression was unaffected in OTUB1$^{-/-}$ cells, multimerization of MAVS was abolished in OTUB1$^{-/-}$ cells but rescued in those expressing WT OTUB1 (Figure 5E). These data indicate that, in the absence of OTUB1, RIG-I fails to form active oligomeric structures, impeding recruitment of the signaling complex, MAVS multimerization, and IRF3 dimerization. To exclude involvement of OTUB1 downstream of MAVS in the RIG-I signaling cascade, we transfected MAVS in OTUB1$^{-/-}$ HEK293T cells in a dose-dependent manner and exposed them to poly(I:C) treatment. MAVS oligomers could form at very high concentrations even in the absence of OTUB1 and were accompanied by IRF3 dimerization, confirming that OTUB1 did not affect signaling downstream of MAVS oligomerization (Figure S3A).

In Vitro Reconstitution of OTUB1-Dependent IRF3 Dimerization Activity from Mitochondrial and Cytosolic Fractions

OTUB1 belongs to the ovarian tumor (OTU) family of cysteine proteases and specifically removes K48-linked polyubiquitin chains (Edelmann et al., 2009; Wang et al., 2009). It also functions non-catalytically by binding E2 enzymes that can either inhibit ubiquitylation or stimulate K48 DUB activity, depending on the concentration of free ubiquitin (Wiener et al., 2012). To determine the mechanism of OTUB1-dependent regulation of the RIG-I pathway, we reconstituted IRF3 dimerization in a cell-free system composed of purified RIG-I, mitochondria, [^{35}S]IRF3, and cytosol preparations from cells expressing OTUB1 variants (Figure 6A). RIG-I purified from either poly(I:C)-treated or IAV-infected cells could support IRF3 dimerization when incubated with cytosol and ATP (Figure 6B). Using this assay, we tested different cytosolic preparations for their ability to dimerize IRF3 (Figures 6C and 6D). Cytosol from OTUB1$^{-/-}$ cells failed to induce IRF3 dimerization. Although cytosol expressing the WT or S16A (cytosolically enriched) could rescue this defect, those expressing mutants defective in forming the E2-repressive complex (D88A) or restricted to the nuclear fraction (S16E) failed to induce IRF3 dimerization. Interestingly, with the catalytically dead mutant C91S, there was only a partial loss of IRF3 dimerization, suggesting that either the enzymatic activity of OTUB1 is not required or that redundancy with other cytosolic DUBs can partially compensate for this activity. Collectively, these data indicate that the non-canonical function of forming the E2-repressive complex rather than the enzymatic activity of OTUB1 has a more profound effect on IRF3 activation.

To analyze this further, we performed time course analyses on IRF3 dimerization with cytosol from OTUB1$^{-/-}$ cells or from those expressing its mutant variants. Rapid IRF3 dimerization occurred with the WT and the S16A mutant, as noted above, but not with the S16E and D88A mutant constructs. Cytosol expressing the catalytically dead C91S mutant displayed significantly slower kinetics of IRF3 dimerization but was able to partially support this activity at later time points (Figure 6E). Collectively, our data indicate that formation of the E2∼OTUB1 repressive complex is a critical step in RIG-I-dependent IRF3 activity. To validate these results in intact cells, we transduced OTUB1$^{-/-}$ A549 cells expressing the IRF luciferase reporter with either the WT, C91S, or D88A constructs. These cells were then stimulated with either poly(I:C) or infected with the H1N1(pdm) strain. In line with our findings from the cell-free *in vitro* assay, C91S was able to partially rescue IRF activity whereas D88A did not (Figures 6F and 6G). Production of IFN-I from these cells was also measured and reflected the phenotype for IRF3 dimerization (Figure 6H).

To identify which E2 was being inhibited by OTUB1, we tested UBC13 and UBCH5(a–c), all of which are known to bind OTUB1. We generated a set of cytosolic preparations from cells depleted in the corresponding E2s (Figure 6I) and reconstituted them in the *in vitro* IRF3 dimerization assay. Although UBC13-deficient cytosol was devoid of activity, UBCH5c deficiency displayed even faster IRF3 dimerization kinetics than that from WT cells (Figure 6J). These data recapitulated OTUB1-dependent IRF3 activity and indicated that formation of the UBCH5c∼OTUB1 repressive complex contributes to activating the RIG-I signaling pathway. However, we cannot categorically rule out involvement of UBCH5a/b because residual activities in the cytosol fractions could be sufficient for ubiquitylation.

Our data suggest that OTUB1 prevents accumulation and conjugation of K48 polyubiquitin chains to RIG-I. Therefore, altering the local concentrations of K48 and K63 polyubiquitin would, in principle, regulate association of RIG-I with K63 polyubiquitin and subsequent IRF3 dimerization. To test this hypothesis, cytosolic fractions from cells expressing WT OTUB1 were supplemented with a defined concentration of ubiquitin containing either K63 alone (Ub2–Ub7) or varying ratios of K48:K63 chains to measure IRF3 dimerization. In line with our hypothesis, increasing concentrations of K48 polyubiquitin resulted in a systematic reduction in the kinetics of IRF3 dimerization (Figure 6K). At K48:K63 ratios of more than 2:1, the rate of IRF3 dimerization decreased significantly, indicating that concentrations of free polyubiquitin chains can determine optimal ubiquitylation of RIG-I and regulate the magnitude of the signal transduction cascade.

(C) Activation of NF-κB was measured in mock- and IAV-infected cells (WT, OTUB1$^{-/-}$, or rOTUB1) by the appearance of phosphorylated p65.
(D) Activation of NF-κB in A549^{dual} cells (WT, OTUB1$^{-/-}$, RIG-I$^{-/-}$, or OTUB1$^{-/-}$RIG-I$^{-/-}$ double knockout) infected with different strains of IAV was measured by secreted alkaline phosphatase absorbance at 620 nm.
(E) Activation of IRF3 in cells (described in D) was measured by luciferase luminescence.
(F) NF-κB and IRF3 activities in ZIKV-infected cells (MOI 1.0) was measured at the indicated time intervals using the same readouts as in (D) and (E).
(G) NF-κB and IRF3 activities in EMCV-infected cells infected at MOI 1.0 for the indicated time intervals and measured as in (D) and (E).
(H) A549^{dual} cells were stimulated with 10 μg/mL of 2′3′-cGAMP. NF-κB induction was determined by QUANTI-blue by measuring optical density (OD) at 620 nm; IRF induction was determined by QUANTI-Luc in a luminometer.
(I) Cells in (H) were stimulated with 10 μg/mL of linearized 2′3′-GAMP as a negative control.
All curve fits were generated with data from at least 3 independent experiments. The images in (B) and (C) are representative of at least 3 independent biological replicates.

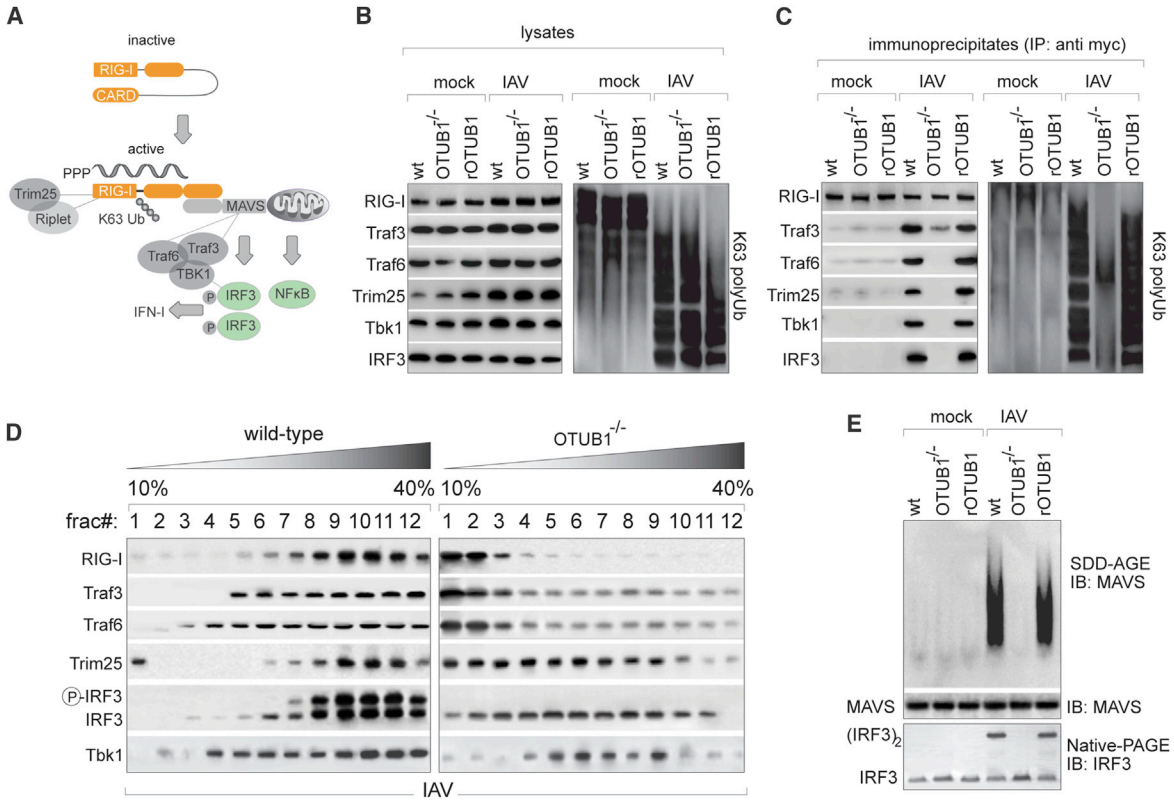

Figure 5. Disassembly of the RIG-I Signaling Complex in the Absence of OTUB1

(A) Schematic of the activated RIG-I complex and known interactors of the pathway.

(B) A549 cells stably transduced with myc-RIG-I were genome edited to express either WT, OTUB1$^{-/-}$, or rOTUB1 and exposed to mock or IAV infection. Signaling molecules were detected by immunoblotting in lysates prepared from mock- and IAV-infected cells (left panel); the presence of K63 polyubiquitin chains in the lysates was measured using anti-K63 antibodies (right panel).

(C) IP of RIG-I using anti-myc from mock- and IAV-infected cells described in (B) was resolved by SDS-PAGE and immunoblotted for co-purifying components (left panel) and K63 ubiquitin chains (right panel),

(D) Lysates from WT or OTUB1$^{-/-}$ cells infected with IAV was resolved by velocity sedimentation on glycerol gradients (10%–40% (w/v)); collected fractions were desalted, resolved by SDS-PAGE, and detected by immunoblotting for components of the RIG-I complex.

(E) Lysates from (B) were also resolved by semidenaturing agarose gels (SDD-AGE) to visualize MAVS oligomerization in mock- and IAV-infected cells (top panel), SDS-PAGE to measure total MAVS levels (center panel), and native PAGE to measure IRF3 dimerization (bottom panel).

To detect RIG-I∼K63 association under the conditions described above, we immunoprecipitated myc-RIG-I from the reaction mix and immunoblotted with linkage-specific anti-ubiquitin antibodies. The extent of co-precipitating ubiquitin chains reflected those of the K48:K63 ratios and downstream IRF3 activities (Figure 6L). Furthermore, for all cytosol preparations that displayed attenuated IRF3 dimerization, an increase in K48 polyubiquitin association with RIG-I was noted compared with cytosol expressing WT OTUB1 (Figure 6M). Our data indicate that high local concentrations of K63 polyubiquitin are maintained by OTUB1 activity to ensure optimal RIG-I-dependent immune signaling. To validate OTUB1-dependent K48-linked ubiquitylation of RIG-I in intact cells, we co-transfected HA-tagged ubiquitin with increasing plasmid concentrations of OTUB1 in OTUB1$^{-/-}$ HEK293T cells expressing myc-RIG-I. A dose-dependent decrease in K48 polyubiquitin chains co-precipitating with RIG-I was noted with increasing concentrations of OTUB1 (Figure S4).

OTUB1 Is Targeted for Proteasomal Degradation by IAV NS1

The reduction in steady-state levels of OTUB1 in IAV-infected cells at later time points (Figures 2B–2D) suggested that it is very likely targeted for degradation. Among the viral factors, we identified PB2 and NS1 in the BioID assay (Figure 3D), both of which are known to antagonize host immune responses (Gack et al., 2009; Graef et al., 2010; Mibayashi et al., 2007). We transfected PB2 and NS1 proteins of IAV to test which of them mediated OTUB1 degradation. Expression of NS1 alone was sufficient to reduce the steady-state levels of OTUB1 (Figure 7A). This was further validated by imaging viral NS1 and OTUB1 in IAV-infected cells, which displayed mutually exclusive expression characteristics (Figure 7B). To investigate the turnover of the newly synthesized pool of OTUB1, we first performed pulse-chase assays in [^{35}S]cysteine/methionine ([^{35}S]cys/met)-labeled cells expressing either the WT or C91S mutant of OTUB1. Cells were infected with either WT PR8 IAV or its recombinant mutant strains, one lacking NS1 (ΔNS1) and

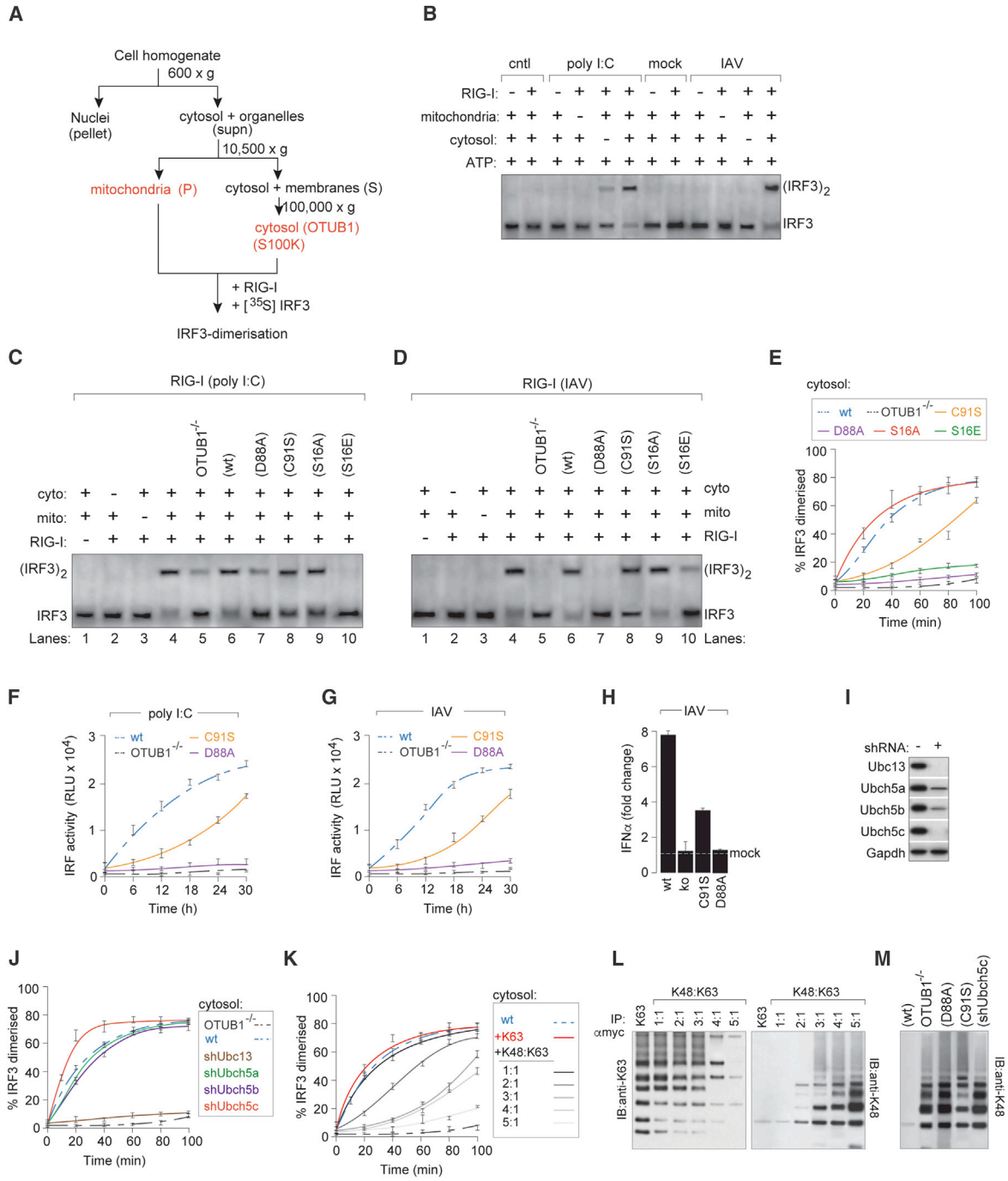

Figure 6. *In Vitro* Reconstitution of OTUB1-Dependent IRF3 Dimerization

(A) Schematic for purification of cytosol and mitochondrial membranes for the reconstitution assay.

(B) IRF3 dimerization was reconstituted with myc-tagged RIG-I isolated from either IAV-infected or poly(I:C)-treated cells, purified with c-*myc* peptide, and compared with mock-infected or untreated cells. The reaction mixture contained mitochondria, cytosolic extracts, ATP, [^{35}S]IRF3, and RIG-I. Dimerization of IRF3 was analyzed by native gel electrophoresis after incubation for 120 min.

(C) Cytosolic extracts were prepared from OTUB1$^{-/-}$ cells or reconstituted with WT, D88A, C91S, S16A, S16E mutants to test for their ability to induce IRF3 dimerization in the assay described in (B), with RIG-I isolated from poly(I:C)-treated cells.

(D) Same as (C), except RIG-I was isolated from IAV-infected cells.

(E) Time courses of IRF3 activation performed with cytosolic extracts as described in (C) and (D) using the assay described in (B). Quantitation of IRF3 dimers was calculated as a percentage of the total from histogram plots generated by ImageJ densitometric analyses. Curve fitting was performed with data obtained from at least 3 independent experiments. Error bars represent mean ± S.D.

(legend continued on next page)

another carrying a mutant NS1, lacking its effector domain (mNS1). At the indicated time intervals, OTUB1 was immunoprecipitated and detected by autoradiography. Newly synthesized WT OTUB1 underwent rapid degradation in the presence of PR8 (WT) but not with either PR8 (ΔNS1) or mNS1. The stability of catalytically dead OTUB1 (C91S), on the other hand, was not affected despite equivalent expression of NS1 (Figure 7C). NS1-dependent degradation of OTUB1 was also validated with the H1N1(pdm) strain (Figure S5).

To further examine this effect, we transfected NS1 into cells expressing OTUB1 variants and compared them with control cells transfected with the empty vector. Both the WT and cytosol-localized mutant (S16A) were rapidly degraded in the presence of NS1, whereas the catalytic mutant (C91S) and that deficient in binding to E2 (D88A) and nucleus localized (S16E) remained unaffected (Figure 7D).

To test whether NS1-mediated degradation of OTUB1 was a universal phenomenon, we expressed NS1 variants from different strains of IAV. WT NS1 from PR8 was able to rapidly degrade OTUB1, whereas a mutant lacking the effector domain had no effect on OTUB1 turnover. Expression of NS1 from all strains (H1N1(pdm), H3N2, and H9N2), except H5N1, were able to degrade newly synthesized OTUB1 (Figure 7E). NS1-mediated degradation of OTUB1 was blocked upon proteasomal inhibition by MG132 (Figure 7F). Collectively, our data indicate that OTUB1-dependent activation of RIG-I is impeded by the presence of IAV NS1 by facilitating its proteasomal degradation.

DISCUSSION

RLRs are critical cytosolic sensors for pathogen-associated molecular patterns (PAMPs) and play key roles in prompting innate immune responses against microbial infection. Virus sensing triggers RIG-I tetramerization, K63 ubiquitylation, and recruitment of signaling adaptor molecules, which culminate in NF-κB and IRF activation to induce expression of antiviral genes. Not surprisingly, during the course of their co-evolution, viruses have acquired strategies to subvert such immune mechanisms by various means, such as exploiting host factors to their own advantage or triggering their degradation to dysregulate intracellular processes.

Ubiquitylation is strategically positioned to fine-tune the magnitude and duration of immune signaling cascades and, therefore, is also an attractive target for viral subversion mechanisms (Ribet and Cossart, 2010). In this study, we profiled DUBs that are activated upon IAV infection and identified OTUB1 as a critical regulator of RIG-I that is targeted for degradation by IAV NS1. OTUB1 was IFN inducible, associated with the RIG-I complex (specifically the active oligomeric pool at the mitochondrial membranes), and targeted for proteasomal degradation during IAV infection. Deletion of OTUB1 resulted in impaired IRF3 and NF-κB activation equivalent to that of RIG-I deletion with all tested strains of IAV and could be rescued by reconstitution with the WT variant into the deletion background.

To determine the mechanism of OTUB1-dependent RIG-I activation, we adopted a cell-free system of IRF3 dimerization (Zeng et al., 2010) reconstituted from purified RIG-I, mitochondria, and cytosol expressing OTUB1 variants. Previous studies have reported that OTUB1 specifically hydrolyses K48 polyubiquitin but also binds and sequesters E2 enzymes to inhibit ubiquitylation (Herhaus et al., 2013; Sun et al., 2012). Mutation in its catalytic cysteine (C91S) abolishes its enzymatic function. The D88A mutation blocks its ability to bind to E2 enzymes (Sun et al., 2012), and perturbation of its phosphorylation alters it subcellular distribution; S16A is cytosolic, whereas S16E is nucleus localized (Figure S1; Herhaus et al., 2015). Cytosol fractions from cells deficient in OTUB1 did not support IRF3 dimerization in the cell-free reconstituted assay. Among cytosol preparations expressing the various mutants, WT OTUB1 was proficient in supporting IRF3 activation, and C91S displayed significantly slower kinetics, suggesting that this activity is probably rescued by other cytosolic DUBs; however, with the D88A mutant, IRF3 activity was completely blocked, indicating that both the DUB activity and E2-repressive function of OTUB1 are employed in the RIG-I signaling pathway.

To determine which E2s might function in this cascade, we generated cells depleted of the known E2 interactors of OTUB1, UBCH5(a–c), and UBC13. Depletion of UBC13, which functions in TRIM25-dependent K63 ubiquitylation of RIG-I, resulted in abrogation of IRF3 activity, whereas that of UBCH5c in particular allowed rapid IRF3 dimerization, reminiscent of OTUB1 rescue assays. Our data suggest that OTUB1

(F and G) OTUB1$^{-/-}$ A549^{dual} cells were reconstituted with either WT, C91S, or D88A constructs of OTUB1 and stimulated with (F) poly(I:C) or (G) H1N1 (MOI 1.0) for the indicated time intervals. IRF induction was determined by QUANTI-Luc in a luminometer.

(H) IFN production was measured from IAV-infected (H1N1(pdm), MOI 1.0) WT and OTUB1$^{-/-}$ A549 cells or those expressing either C91S or D88A mutants in the OTUB1$^{-/-}$ background. Supernatants were collected at 24 h after infection and secreted IFN-α was measured by ELISA or fluorescence-activated cell sorting (FACS) using a bead-based assay for cytokine detection. Error bars represent mean ± S.D. from at least three independent experiments.

(I) The role of E2 enzymes in OTUB1-dependent IRF3 dimerization. Depletion of UBC13 and UBCH5(a–c) was performed in A549 cells using shRNA targeting the corresponding enzymes. Cell lysates were immunoblotted with antibodies against the endogenous proteins to confirm their depletion.

(J) Cytosolic extracts generated from WT or OTUB1$^{-/-}$ cells or from those depleted in the E2 enzymes from (I) were reconstituted to measure their ability to support IRF3 dimerization using the assay described in (E).

(K) Dependence of OTUB1-dependent IRF3 dimerization on the ratio of K48:K63 ubiquitin chains. The reaction mixture in the IRF3 dimerization assay was supplemented with either 10 μM K63 polyubiquitin (Ub2–Ub7) alone or with increasing amounts of K48 polyubiquitin (Ub2–Ub7) to vary the ratio with a constant total concentration of 10 μM.

(L) Polyubiquitylation status of RIG-I in the reaction mix was determined at the endpoint of IRF3 dimerization time courses in (K) by IP on anti-myc antibodies and immunoblotting with linkage-specific anti-Ub.

(M) K48 polyubiquitin association with RIG-I was determined as in (L) in reactions with cytosol preparations from WT, OTUB1$^{-/-}$, D88A, C91S, and shUbch5c-expressing cells.

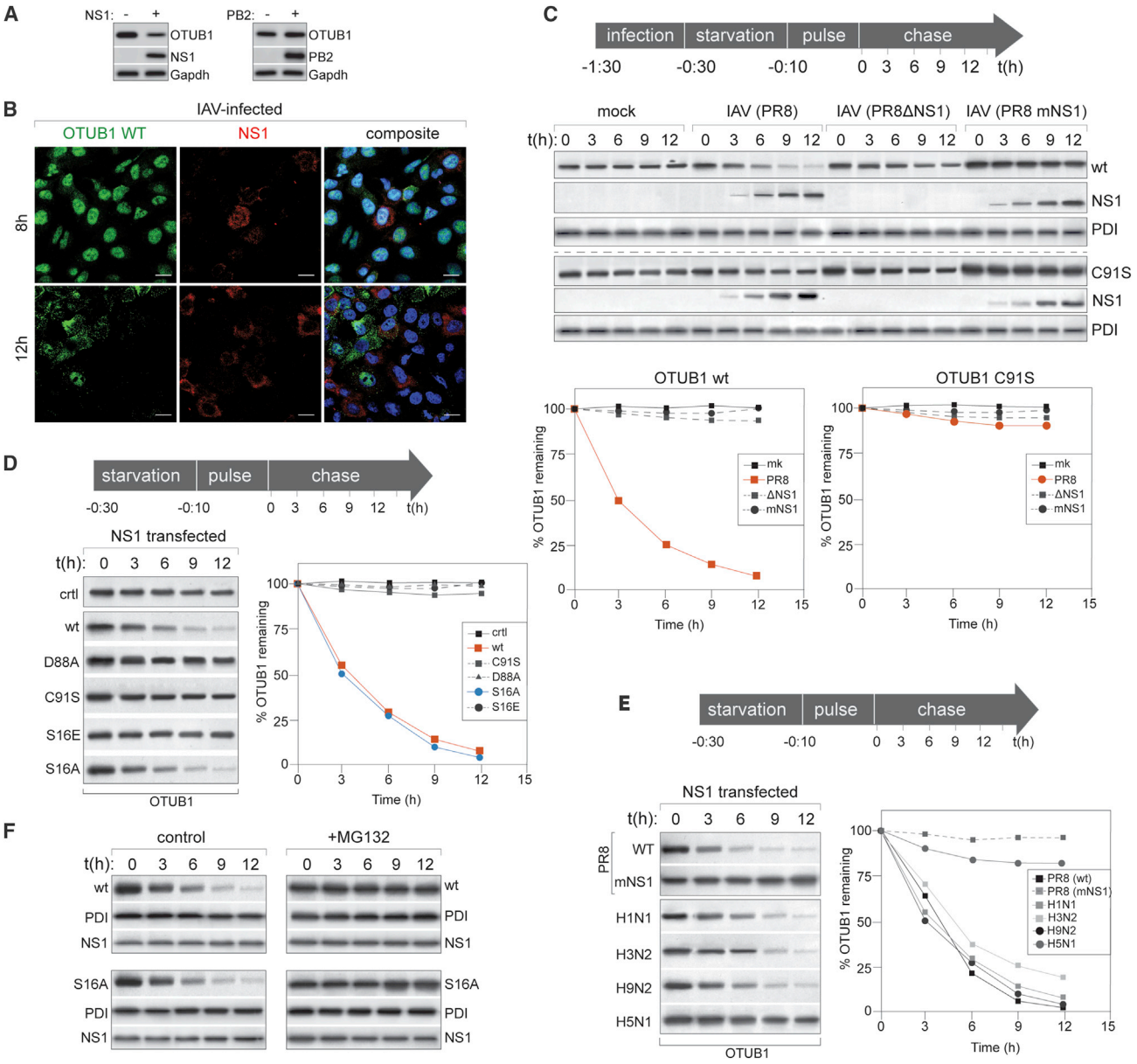

Figure 7. Influenza NS1 Triggers Proteasomal Degradation of OTUB1

(A) Steady-state levels of endogenous OTUB1 was measured in A549 cells transfected with either IAV NS1 or PB2.

(B) Expression of OTUB1 and IAV NS1 is anti-correlated. Confocal imaging was performed on cells infected with IAV (H1N1(pdm)). 8 h and 12 h after infection, cells were fixed and stained to visualize distribution of OTUB1 and NS1. Scale bar, 10 μm. Images are representative of more than 3 independent experiments.

(C) WT OTUB1 but not the C91S catalytic mutant is degraded by IAV NS1. Pulse-chase analyses were performed with OTUB1$^{-/-}$ cells expressing either WT OTUB1 or C91S mutant and infected with either PR8 (WT), PR8 (ΔNS1), or PR8 (mNS1), which lacks the effector domain. Infected cells were pulsed with [^{35}S]cys/met and chased for the indicated time intervals. At each time point, OTUB1 (WT or C91S) was immunoprecipitated and detected by autoradiography. The amount of remaining OTUB1 was calculated using densitometry as a percentage of total at the 0 time point, normalized to 100%. Expression of NS1 was measured by IP on anti-NS1 antibodies, followed by autoradiography. Expression of PDI was measured as a loading control.

(D) OTUB1$^{-/-}$ cells expressing either the WT or mutant variants were transfected with either empty vector (control [crtl]) or IAV NS1, and pulse-chase assays were performed to measure OTUB1 turnover as described in (B).

(E) NS1 constructs from different IAV strains, as indicated, were transfected into cells for pulse-chase analyses as described in (B) and (C).

(F) NS1 from PR8 was transfected into cells expressing the WT or S16A variant of OTUB1 and left untreated or treated with 5 μM MG132 for 4 h to inhibit proteasomal degradation. Pulse-chase analyses of OTUB1 turnover was determined as described in (B) and (C). Expression of PDI and NS1 was measured by IP on anti-PDI and anti-NS1 antibodies, followed by autoradiography.

participates by a dual mechanism to enable RIG-I activation; first via its conventional deubiquitylating activity and also by inhibition of E2 enzymes, most likely Ubch5c, although we cannot exclude involvement of other E2s. This achieves two outcomes: (1) it creates an optimal concentration of K63 polyubiquitin chains, and (2) stabilizes and inhibits proteasomal degradation of the RIG-I complex. The two distinct activities are likely regulated by the local concentrations of K48 and K63 polyubiquitin chains. A combined effect of hydrolyzing K48 chains and inhibiting UBCH5c-mediated K48 ubiquitylation of RIG-I would therefore provide tight regulation of RIG-I activation and signal amplification upon infection. Not surprisingly, expression of the multifunctional IAV NS1 alone was sufficient to downregulate this phenomenon through proteasomal degradation of OTUB1. Interestingly, NS1-mediated degradation was specific to WT OTUB1 but not the C91S catalytic mutant. This could occur because of failure of NS1 interaction with OTUB1 (C91S) or of the of the putative E3 ligases that recognize/ubiquitylate OTUB1 (C91S). This study therefore underscores the intricate and complex dynamic that exists in the utilization of DUBs in the host-pathogen arms race. A mechanistic understanding of its function in the context of infection provides fundamental insights into regulation of cell signaling and viral evasion strategies.

STAR★METHODS

Detailed methods are provided in the online version of this paper and include the following:

- KEY RESOURCES TABLE
- LEAD CONTACT AND MATERIALS AVAILABILITY
- EXPERIMENTAL MODEL AND SUBJECT DETAILS
  - Cell Lines
  - Primary cell cultures
  - Virus strains
- METHOD DETAILS
  - Virus infections
  - Screen for isolation of deubiquitylases
  - Immunoprecipitation and mass spectrometry
  - Isolation of OTUB1 partners in mock and virus infected cells
  - Quanti-blue SEAP Phosphatase assay
  - Quanti-luc luciferase assay
  - Transient transfections and lentiviral transductions
  - Pulse-chase analysis of OTUB1 turnover
  - Generation of knock-out and knock-down cells
  - *In vitro* reconstitution of IRF3 dimerization
  - Glycerol gradient analyses
  - Immunofluorescence assays
- QUANTIFICATION AND STATISTICAL ANALYSIS
- DATA AND CODE AVAILABILITY

SUPPLEMENTAL INFORMATION

Supplemental Information can be found online at https://doi.org/10.1016/j.celrep.2020.01.015.

ACKNOWLEDGMENTS

This work was funded by Research Grants Council (GRF) grants 17113915 and 17112617 and partially supported by Health and Medical Research Funds (16150592), a theme-based research grant from the Research Grants Council (project T11-705/14N), and PTR (546) from Institut Pasteur. S.S. is supported by the Croucher Foundation. The authors thank Michael Weekes and Benedikt Kessler for suggestions regarding mass spectrometry analyses.

AUTHOR CONTRIBUTIONS

S.S. was responsible for the overall design of the study. A.S.J., E.B., R.M.-M., C.K.-P.M., H.H.W., A.L.Q., and Q.W.T. performed the experiments. A.W.H.C., R.M.-M., L.L.M.P., C.D., and A.G.-S. were involved in generation and characterization of constructs, recombinant viruses, and cell lines critical to the study.

DECLARATION OF INTERESTS

The authors declare no competing interests.

Received: May 22, 2019
Revised: October 21, 2019
Accepted: January 2, 2020
Published: February 4, 2020

REFERENCES

Biquand, E., Poirson, J., Karim, M., Declercq, M., Malausse, N., Cassonnet, P., Barbezange, C., Straub, M.L., Jones, L., Munier, S., et al. (2017). Comparative Profiling of Ubiquitin Proteasome System Interplay with Influenza A Virus PB2 Polymerase Protein Recapitulating Virus Evolution in Humans. MSphere *2*, 19428.

Cadena, C., Ahmad, S., Xavier, A., Willemsen, J., Park, S., Park, J.W., Oh, S.W., Fujita, T., Hou, F., Binder, M., and Hur, S. (2019). Ubiquitin-Dependent and -Independent Roles of E3 Ligase RIPLET in Innate Immunity. Cell *177*, 1187–1200.e16.

Catrysse, L., Vereecke, L., Beyaert, R., and van Loo, G. (2014). A20 in inflammation and autoimmunity. Trends Immunol. *35*, 22–31.

Chan, R.W.Y., Chan, L.L.Y., Mok, C.K.P., Lai, J., Tao, K.P., Obadan, A., Chan, M.C.W., Perez, D.R., Peiris, J.S.M., and Nicholls, J.M. (2017). Replication of H9 influenza viruses in the human ex vivo respiratory tract, and the influence of neuraminidase on virus release. Sci. Rep. *7*, 6208.

Düwel, M., Welteke, V., Oeckinghaus, A., Baens, M., Kloo, B., Ferch, U., Darnay, B.G., Ruland, J., Marynen, P., and Krappmann, D. (2009). A20 negatively regulates T cell receptor signaling to NF-kappaB by cleaving Malt1 ubiquitin chains. J. Immunol. *182*, 7718–7728.

Edelmann, M.J., Iphöfer, A., Akutsu, M., Altun, M., di Gleria, K., Kramer, H.B., Fiebiger, E., Dhe-Paganon, S., and Kessler, B.M. (2009). Structural basis and specificity of human otubain 1-mediated deubiquitination. Biochem. J. *418*, 379–390.

Fan, Y., Mao, R., Yu, Y., Liu, S., Shi, Z., Cheng, J., Zhang, H., An, L., Zhao, Y., Xu, X., et al. (2014). USP21 negatively regulates antiviral response by acting as a RIG-I deubiquitinase. J. Exp. Med. *211*, 313–328.

Fan, Y., Mok, C.K.P., Chan, M.C.W., Zhang, Y., Nal, B., Kien, F., Bruzzone, R., and Sanyal, S. (2017). Cell Cycle-independent Role of Cyclin D3 in Host Restriction of Influenza Virus Infection. J. Biol. Chem. *292*, 5070–5088.

Gack, M.U. (2014). Mechanisms of RIG-I-like receptor activation and manipulation by viral pathogens. J. Virol. *88*, 5213–5216.

Gack, M.U., Shin, Y.C., Joo, C.H., Urano, T., Liang, C., Sun, L., Takeuchi, O., Akira, S., Chen, Z., Inoue, S., and Jung, J.U. (2007). TRIM25 RING-finger E3 ubiquitin ligase is essential for RIG-I-mediated antiviral activity. Nature *446*, 916–920.

Gack, M.U., Albrecht, R.A., Urano, T., Inn, K.S., Huang, I.C., Carnero, E., Farzan, M., Inoue, S., Jung, J.U., and García-Sastre, A. (2009). Influenza A virus NS1 targets the ubiquitin ligase TRIM25 to evade recognition by the host viral RNA sensor RIG-I. Cell Host Microbe *5*, 439–449.

García-Sastre, A., Egorov, A., Matassov, D., Brandt, S., Levy, D.E., Durbin, J.E., Palese, P., and Muster, T. (1998). Influenza A virus lacking the NS1 gene replicates in interferon-deficient systems. Virology *252*, 324–330.

Graef, K.M., Vreede, F.T., Lau, Y.F., McCall, A.W., Carr, S.M., Subbarao, K., and Fodor, E. (2010). The PB2 subunit of the influenza virus RNA polymerase affects virulence by interacting with the mitochondrial antiviral signaling protein and inhibiting expression of beta interferon. J. Virol. *84*, 8433–8445.

Hale, B.G., Steel, J., Manicassamy, B., Medina, R.A., Ye, J., Hickman, D., Lowen, A.C., Perez, D.R., and García-Sastre, A. (2010). Mutations in the NS1 C-terminal tail do not enhance replication or virulence of the 2009 pandemic H1N1 influenza A virus. J. Gen. Virol. *91*, 1737–1742.

Herhaus, L., Al-Salihi, M., Macartney, T., Weidlich, S., and Sapkota, G.P. (2013). OTUB1 enhances TGFβ signalling by inhibiting the ubiquitylation and degradation of active SMAD2/3. Nat. Commun. *4*, 2519.

Herhaus, L., Perez-Oliva, A.B., Cozza, G., Gourlay, R., Weidlich, S., Campbell, D.G., Pinna, L.A., and Sapkota, G.P. (2015). Casein kinase 2 (CK2) phosphorylates the deubiquitylase OTUB1 at Ser16 to trigger its nuclear localization. Sci. Signal. *8*, ra35.

Jahan, A.S., Lestra, M., Swee, L.K., Fan, Y., Lamers, M.M., Tafesse, F.G., Theile, C.S., Spooner, E., Bruzzone, R., Ploegh, H.L., and Sanyal, S. (2016). Usp12 stabilizes the T-cell receptor complex at the cell surface during signaling. Proc. Natl. Acad. Sci. USA *113*, E705–E714.

Jiang, X., Kinch, L.N., Brautigam, C.A., Chen, X., Du, F., Grishin, N.V., and Chen, Z.J. (2012). Ubiquitin-induced oligomerization of the RNA sensors RIG-I and MDA5 activates antiviral innate immune response. Immunity *36*, 959–973.

Juang, Y.C., Landry, M.C., Sanches, M., Vittal, V., Leung, C.C., Ceccarelli, D.F., Mateo, A.R., Pruneda, J.N., Mao, D.Y., Szilard, R.K., et al. (2012). OTUB1 co-opts Lys48-linked ubiquitin recognition to suppress E2 enzyme function. Mol. Cell *45*, 384–397.

Kayagaki, N., Phung, Q., Chan, S., Chaudhari, R., Quan, C., O'Rourke, K.M., Eby, M., Pietras, E., Cheng, G., Bazan, J.F., et al. (2007). DUBA: a deubiquitinase that regulates type I interferon production. Science *318*, 1628–1632.

Komander, D., Clague, M.J., and Urbé, S. (2009). Breaking the chains: structure and function of the deubiquitinases. Nat. Rev. Mol. Cell Biol. *10*, 550–563.

Kowalinski, E., Lunardi, T., McCarthy, A.A., Louber, J., Brunel, J., Grigorov, B., Gerlier, D., and Cusack, S. (2011). Structural basis for the activation of innate immune pattern-recognition receptor RIG-I by viral RNA. Cell *147*, 423–435.

Kwasna, D., Abdul Rehman, S.A., Natarajan, J., Matthews, S., Madden, R., De Cesare, V., Weidlich, S., Virdee, S., Ahel, I., Gibbs-Seymour, I., and Kulathu, Y. (2018). Discovery and Characterization of ZUFSP/ZUP1, a Distinct Deubiquitinase Class Important for Genome Stability. Mol. Cell *70*, 150–164.e6.

Lin, D., Zhang, M., Zhang, M.X., Ren, Y., Jin, J., Zhao, Q., Pan, Z., Wu, M., Shu, H.B., Dong, C., and Zhong, B. (2015). Induction of USP25 by viral infection promotes innate antiviral responses by mediating the stabilization of TRAF3 and TRAF6. Proc. Natl. Acad. Sci. USA *112*, 11324–11329.

Liu, H.M., Loo, Y.M., Horner, S.M., Zornetzer, G.A., Katze, M.G., and Gale, M., Jr. (2012). The mitochondrial targeting chaperone 14-3-3ε regulates a RIG-I translocon that mediates membrane association and innate antiviral immunity. Cell Host Microbe *11*, 528–537.

Mali, P., Yang, L., Esvelt, K.M., Aach, J., Guell, M., DiCarlo, J.E., Norville, J.E., and Church, G.M. (2013). RNA-guided human genome engineering via Cas9. Science *339*, 823–826.

Mibayashi, M., Martínez-Sobrido, L., Loo, Y.M., Cárdenas, W.B., Gale, M., Jr., and García-Sastre, A. (2007). Inhibition of retinoic acid-inducible gene I-mediated induction of beta interferon by the NS1 protein of influenza A virus. J. Virol. *81*, 514–524.

Ovaa, H., Kessler, B.M., Rolén, U., Galardy, P.J., Ploegh, H.L., and Masucci, M.G. (2004). Activity-based ubiquitin-specific protease (USP) profiling of virus-infected and malignant human cells. Proc. Natl. Acad. Sci. USA *101*, 2253–2258.

Pauli, E.K., Chan, Y.K., Davis, M.E., Gableske, S., Wang, M.K., Feister, K.F., and Gack, M.U. (2014). The ubiquitin-specific protease USP15 promotes RIG-I-mediated antiviral signaling by deubiquitylating TRIM25. Sci. Signal. *7*, ra3, ra3.

Poon, L.L.M., Song, T., Rosenfeld, R., Lin, X., Rogers, M.B., Zhou, B., Sebra, R., Halpin, R.A., Guan, Y., Twaddle, A., et al. (2016). Quantifying influenza virus diversity and transmission in humans. Nat. Genet. *48*, 195–200.

Rehwinkel, J., Tan, C.P., Goubau, D., Schulz, O., Pichlmair, A., Bier, K., Robb, N., Vreede, F., Barclay, W., Fodor, E., and Reis e Sousa, C. (2010). RIG-I detects viral genomic RNA during negative-strand RNA virus infection. Cell *140*, 397–408.

Reyes-Turcu, F.E., Ventii, K.H., and Wilkinson, K.D. (2009). Regulation and cellular roles of ubiquitin-specific deubiquitinating enzymes. Annu. Rev. Biochem. *78*, 363–397.

Ribet, D., and Cossart, P. (2010). Pathogen-mediated posttranslational modifications: A re-emerging field. Cell *143*, 694–702.

Roux, K.J., Kim, D.I., Raida, M., and Burke, B. (2012). A promiscuous biotin ligase fusion protein identifies proximal and interacting proteins in mammalian cells. J. Cell Biol. *196*, 801–810.

Sanyal, S., Claessen, J.H.L., and Ploegh, H.L. (2012). A viral deubiquitylating enzyme restores dislocation of substrates from the endoplasmic reticulum (ER) in semi-intact cells. J. Biol. Chem. *287*, 23594–23603.

Sanyal, S., Ashour, J., Maruyama, T., Altenburg, A.F., Cragnolini, J.J., Bilate, A., Avalos, A.M., Kundrat, L., García-Sastre, A., and Ploegh, H.L. (2013). Type I interferon imposes a TSG101/ISG15 checkpoint at the Golgi for glycoprotein trafficking during influenza virus infection. Cell Host Microbe *14*, 510–521.

Sun, X.X., Challagundla, K.B., and Dai, M.S. (2012). Positive regulation of p53 stability and activity by the deubiquitinating enzyme Otubain 1. EMBO J. *31*, 576–592.

Te Velthuis, A.J.W., Long, J.C., Bauer, D.L.V., Fan, R.L.Y., Yen, H.L., Sharps, J., Siegers, J.Y., Killip, M.J., French, H., Oliva-Martín, M.J., et al. (2018). Mini viral RNAs act as innate immune agonists during influenza virus infection. Nat. Microbiol. *3*, 1234–1242.

Trompouki, E., Hatzivassiliou, E., Tsichritzis, T., Farmer, H., Ashworth, A., and Mosialos, G. (2003). CYLD is a deubiquitinating enzyme that negatively regulates NF-kappaB activation by TNFR family members. Nature *424*, 793–796.

Valkenburg, S.A., Li, O.T.W., Mak, P.W.Y., Mok, C.K.P., Nicholls, J.M., Guan, Y., Waldmann, T.A., Peiris, J.S.M., Perera, L.P., and Poon, L.L.M. (2014). IL-15 adjuvanted multivalent vaccinia-based universal influenza vaccine requires CD4+ T cells for heterosubtypic protection. Proc. Natl. Acad. Sci. USA *111*, 5676–5681.

Wang, T., Yin, L., Cooper, E.M., Lai, M.Y., Dickey, S., Pickart, C.M., Fushman, D., Wilkinson, K.D., Cohen, R.E., and Wolberger, C. (2009). Evidence for bidentate substrate binding as the basis for the K48 linkage specificity of otubain 1. J. Mol. Biol. *386*, 1011–1023.

Wang, L., Zhao, W., Zhang, M., Wang, P., Zhao, K., Zhao, X., Yang, S., and Gao, C. (2013). USP4 positively regulates RIG-I-mediated antiviral response through deubiquitination and stabilization of RIG-I. J. Virol. *87*, 4507–4515.

Wiener, R., Zhang, X., Wang, T., and Wolberger, C. (2012). The mechanism of OTUB1-mediated inhibition of ubiquitination. Nature *483*, 618–622.

Yoneyama, M., and Fujita, T. (2008). Structural mechanism of RNA recognition by the RIG-I-like receptors. Immunity *29*, 178–181.

Zeng, W., Sun, L., Jiang, X., Chen, X., Hou, F., Adhikari, A., Xu, M., and Chen, Z.J. (2010). Reconstitution of the RIG-I pathway reveals a signaling role of unanchored polyubiquitin chains in innate immunity. Cell *141*, 315–330.

Zhang, J., Lan, Y., Li, M.Y., Lamers, M.M., Fusade-Boyer, M., Klemm, E., Thiele, C., Ashour, J., and Sanyal, S. (2018a). Flaviviruses Exploit the Lipid Droplet Protein AUP1 to Trigger Lipophagy and Drive Virus Production. Cell Host Microbe *23*, 819–831.e5.

Zhang, L., Liu, J., Qian, L., Feng, Q., Wang, X., Yuan, Y., Zuo, Y., Cheng, Q., Miao, Y., Guo, T., et al. (2018b). Induction of OTUD1 by RNA viruses potently inhibits innate immune responses by promoting degradation of the MAVS/TRAF3/TRAF6 signalosome. PLoS Pathog. *14*, e1007067.

STAR★METHODS

KEY RESOURCES TABLE

REAGENT or RESOURCE	SOURCE	IDENTIFIER
Antibodies		
Anti-OTUB1	Abcam	Cat# ab175200
Anti-GAPDH	Abcam	Cat# ab8245; RRID:AB_2107448
Anti-NS1	Santa Cruz	Cat# sc-130568; RRID:AB_2011757
Anti-PB2	Thermo fisher Scientific	Cat# PA5-32220; RRID:AB_2549693
Anti-TRAF3	Abcam	Cat# ab36988; RRID:AB_778570
Anti-UCHL3	Abcam	Cat# ab126703; RRID:AB_11129956
Anti-USP3	Abcam	Cat# ab101473; RRID:AB_10863008
Anti-DUBA	Abcam	Cat# ab176727
Anti-USP25	Abcam	Cat# ab187156
Anti-HA-HRP	Abcam	Cat# ab128131; RRID:AB_11143947
Anti-RIG-I	Abcam	Cat# ab180675
Anti-ubiquitin	Abcam	Cat# ab7780; RRID:AB_306069
Anti-UB-K48	Abcam	Cat# ab140601; RRID:AB_2783797
Anti-UB-K63	Abcam	Cat# ab179434
Bacterial and Virus Strains		
A/WSN/33 (H1N1)	Sanyal et al., 2013	N/A
A/Oklahoma/309/06 (H3N2)	Fan et al., 2017	N/A
A/Oklahoma/323/03 (H3N2)	Fan et al., 2017	N/A
A/Hong Kong/1073/99 (H9N2)	Chan et al., 2017	N/A
A/California/04/2009(H1N1)	Poon et al., 2016	N/A
A/Puerto Rico/8/34 (PR/34)	García-Sastre et al., 1998	N/A
ΔNS1 A/Puerto Rico/8/34 (PR/34)	García-Sastre et al., 1998	N/A
Vaccinia virus wild-type Wyeth strain	Valkenburg et al., 2014	N/A
EMCV	ATCC	VR-1479
ZIKV (*NC-14-5132*)	ATCC	VR-84
Chemocompetent *E. coli* DH5α	Thermo fisher Scientific	Cat# 18265017
Stbl3 bacteria	Thermo fisher Scientific	Cat# C737303
Chemicals, Peptides, and Recombinant Proteins		
DMEM	Sigma Aldrich	Cat# D5523
HEPES	Sigma Aldrich	Cat# H3375
Protein A Sepharose 4B	Thermo Fisher Scientific	Cat# 101041
Blasticidin	Invivogen	Cat# ant-bl-05
Puromycin	Invivogen	Cat# ant-pr-1
Recombinant human Interferon (IFN)-β protein	Sigma-Aldrich	Cat# IF014
Lipopolysaccharides (LPS)	Sigma-Aldrich	Cat #L2762
Triton X-100	Sigma Aldrich	Cat# 93443
10% Normal Goat Serum (NGS)	Thermo Fisher Scientific	Cat# 50062Z
Complete protease inhibitor cocktail	Roche	Cat# 138468
Protein A-agarose (IPA 300)	RepliGen	Cat# IPA300S
M270 streptavidin-coated Dynabeads	Life Technologies	Cat# 65305
Hygromycin B	Roche Applied Science	Cat# 10843555001
ProLong Gold Antifade Mountant	Thermo Fisher Scientific	Cat# P36930
MG132	Sigma Aldrich	Cat#M7449

(*Continued on next page*)

Continued

REAGENT or RESOURCE	SOURCE	IDENTIFIER
Strep-Tactin beads	IBA life sciences	Cat# 2-4090-002
biotin	Sigma Aldrich	Cat# B4501
Dynabeads MyOne Streptavidin C1	Thermo Fisher Scientific	Cat# 65001
TransITLT1 transfection reagent	Mirus	Cat#MIR2304
T4 Ligase	NEB	Cat# M0202S
Critical Commercial Assays		
Ribomax T7 RNA polymerase kit	Promega	Cat# P2077
Renilla Luciferase Assay	Promega	Cat# E2820
MiniBEST Universal RNA Extraction Kit	TAKARA	Cat# 9767
Cytometric Bead Array assay (CBA)	BD PharMingen	Cat#560005
VeriKine Human Interferon Alpha Elisa Kit	PBL Assay Science	Cat# 41100-2
NE-PER Nuclear and Cytoplasmic Extraction Kit	Thermo fisher scientific	Cat# 78833
QUANTI-blue assay	InvivoGen	Cat# rep-qb1
QUANTI-Luc Gold assay	InvivoGen	Cat# rep-qlcg1
Experimental Models: Cell Lines		
Vero E6	ATCC	CRL-1586
MDCK	ATCC	CCL-34
A549 DUAL	Invivogen	N/A
A549 DUAL RIG-I	Invivogen	N/A
A549 DUAL OTUB1$^{-/-}$	This study	N/A
A549 DUAL RIG-I OTUB1$^{-/-}$	This study	N/A
293T	ATCC	CRL-3216
293T OTUB1$^{-/-}$	This study	N/A
A549	ATCC	CCL-185
A549 OTUB1$^{-/-}$	This study	N/A
A549 Myc-birA-OTUB1	This study	N/A
A549 OTUB1ovrexp	This study	N/A
A549 HA-birA- OTUB1	This study	N/A
Primary human lung epithelial cells	ATCC	PCS-301-010
Oligonucleotides		
GGGCTTCACTGAATTCACAA (sgRNA)	This study	N/A
Recombinant DNA		
pSpCas9(BB)-2A-Puro (PX459) V2.0	García-Sastre et al., 1998	Addgene plasmid # 62988)
OTUB1-PX459	This study	N/A
pcDNA3.1 mycBio-ID	Roux et al., 2012	Addgene plasmid #36047
pcDNA3.1 MCS-BirA(R118G)-HA	Roux et al., 2012	Addgene plasmid #36047
BirA-OTUB1-HA	This study	N/A
BirA-OTUB1-MYC	This study	N/A
OTUB1 (C91S)	This study	N/A
OTUB1 (D88A)	This study	N/A
OTUB1 (S16A)	This study	N/A
OTUB1 (S16E)	This study	N/A
Myc-tagged RIG-I	Te Velthuis et al., 2018	N/A
OTUB1-pOPINK	Addgene	Addgene plasmid #61420)
OTUB1*-pOPINB	Addgene	Addgene plasmid #65441)
pLenti6/V5-OTUB1	This study	N/A
pLenti6/V5-DEST	Zhang et al., 2018a	Thermofisher plasmid # V49610
NS1 A/Puerto Rico/8/34 (PR/34)	Hale et al., 2010	N/A

(*Continued on next page*)

Continued

REAGENT or RESOURCE	SOURCE	IDENTIFIER
NS1 A/California/04/09 NS1 (Cal/09)	Hale et al., 2010	N/A
Strep-PB2 (from H1N1 WSN, H1N1 pdm09, H3N2)	Biquand et al., 2017	N/A
pRK5-HA-Ubiquitin-K48	Addgene	Addgene Plasmid 17605
HA-ub-K63	Addgene	Addgene Plasmid 17606
HA-ubiquitin	Addgene	Addgene Plasmid 18712
Software and Algorithms		
Prism 8.0	GraphPad Software	https://www.graphpad.com/scientific-software/prism/
ImageJ	NIH	https://imagej.net/ImageJ
ZEN confocal software	Zeiss	https://imagej.net/Fiji
CRISPR RGEN Tool Cas-OFFinder	Cas-OFFinder	http://www.rgenome.net/cas-offinder
RStudio 1.2.5001	RStudio, Inc	https://rstudio.com
Ingenuity Pathway Analysis software	QIAGEN	https://www.qiagenbioinformatics.com/products/ingenuity-pathway-analysis/

LEAD CONTACT AND MATERIALS AVAILABILITY

Further information and requests on reagents and resources should be directed to and will be fulfilled by the lead contact, Sumana Sanyal (sanyal@hku.hk).

All unique/stable reagents generated in this study are available from the Lead Contact with a completed Materials Transfer Agreement.

EXPERIMENTAL MODEL AND SUBJECT DETAILS

Cell Lines

The following cell lines were used in this study: A549 cells (human; sex: male; ATCC-CCL-185), A549^{dual} (human; sex: unspecified; Invivogen a549d-nfis), HEK293T (human; sex: unspecified) and Vero E6 cells (*Cercopithecus aethiops;* sex: unspecified) were obtained from commercial sources noted in the Key Resources Table and gender of the cell line was not a consideration in the study. Cells were maintained in DMEM or EMEM supplemented with 10% FBS as specified by the manufacturer.

Primary cell cultures

Primary lung epithelial cells (human; sex: batch-specific; ATCC-PCS-300-010) were maintained according to the manufacturer's protocol.

Virus strains

The following virus strains were used in this study: Influenza A/WSN/33 (H1N1), *A/Oklahoma/309*/06 (H3N2), A/Oklahoma/323/03 (H3N2), A/Hong Kong/1073/99 (H9N2), A/California/04/09 (H1N1 pandemic), A/Hong Kong/483/1997 (483/H5N1), A/Puerto Rico/8/34 (PR/34), ΔNS1 A/Puerto Rico/8/34 (PR/34), Zika virus (NC-14-5132), Vaccinia (Wyeth) and EMCV. Influenza viruses were propagated in Madin Darby canine kidney (MDCK) cells in minimum essential medium (MEM) supplemented with 0.3% bovine serum albumin (BSA) in the presence of 1 μg/ml tosylphenylalanyl chloromethyl ketone (TPCK)-treated trypsin (Thermo Scientific), 1% (v/v) penicillin/streptomycin (Sigma-Aldrich). Supernatants from the virus cultures were harvested three days post-infection. In order to maintain the homogeneity of the viruses, they were propagated with limited passage number and seed stocks of viruses were prepared for future propagation. Virus stocks were aliquoted and stored at −80°C. Viral titers were calculated using plaque assays. ZIKV (NC-14-5132) and *Vaccinia* virus Wyeth *strain* were titrated by determining the tissue culture infective dose 50% ($TCID_{50}$/ml) in Vero E6 cells challenged with 10-fold serial dilutions of infectious supernatants for 90 min at 37°C. EMCV was maintained according to the manufacturer's protocol.

METHOD DETAILS

Virus infections

A549/ Vero/ 293T cells were seeded in 6-well plates with the seeding density of 0.8 X 10^6 cells per well one day before the experiment. Cells were infected with viruses at a multiplicity of infection (MOI) of 4 (single cycle) or 0.01 (multi-cycle growth). After an hour of

adsorption, the viral inoculum was discarded, and infected cells were then washed with PBS and cultured in Opti-MEM added with TPCK-treated trypsin (0.5-1 μg/ml) in a 37°C incubator. Supernatants, cell lysates and RNA were harvested at indicated time points, cleared by centrifugation and stored at −80°C until ready to use.

RT-qPCR assay to measure virus infection

Total RNA was extracted from cells using minibest universal RNA extraction kit (Takara) according to the manufacturer's manual. 1μg of total RNA was used for the following reverse transcription assays. For the quantification of vRNA, 10 μM of vRNA specific primer complementary to the 3′ end of vRNA and 10 μM of β-actin specific primer complementary to the 3′ end of β-actin gene was used together with SuperScript III Reverse Transcriptase (Invitrogen); while for mRNA measurement 500 ng of oligo-dT primer was used in another reverse transcription reaction. To determine the gene copy number of vRNA and mRNA from M gene, a SYBR Green based real-time PCR method (Roche) was used, and the number of β-actin mRNA was used to normalize the total RNA concentration between different samples. The PCR experiments were performed using the LightCycler system 480 (Roche). A reaction mix of 20 μl was composed of 1 μl of each gene-specific primer at 10 μM, 10 μl of SYBR Green master mix, 5 μl of 10-fold diluted cDNA and 3 μl of distilled water. The amplification program was as it follows: 95°C for 5 min, followed by 45 cycles of 95°C for 10 s, 60°C for 10 s and 72°C for 10 s. The specificity of the assay was confirmed by melting-curve analysis at the end of the amplification program. The primers for M gene and β-actin detection are described in the Key Resources Table.

Plaque assays

MDCK cells were seeded in 6-well plates with a seeding density of 1 X 10^6 per well. The following day confluent MDCK plates were washed twice with PBS. 100 μL of 10-fold serial dilutions of supernatants were added to monolayers for adsorption. After one h of incubation at 37°C, the viral inoculum was discarded, and overlaid with MEM containing 1% agarose and 1 μg/mL TPCK-treated trypsin, and incubated inverted at 37°C for 3 days. Cells were fixed with 10% formalin in PBS overnight. and stained with 1% crystal violet solution containing 20% ethanol. Plaques were counted and recorded after drying the plates.

Minigenome viral replicon assay

Cells were transfected in 12-well plates with plasmids encoding PB1, PB2, PA, and NP proteins (320 ng of NP, 160 ng [each] of PB1 and PB2, and 40 ng of PA), together with a plasmid expressing negative-sense firefly luciferase using the Lipofectamine 2000 transfection reagent (Invitrogen), and incubated at 37°C. Twenty hours after transfection, cells were lysed with 300 μL of passive lysis buffer (Promega), and firefly luciferase activity was measured using a luminometer.

Screen for isolation of deubiquitylases

~1 × 10^7 cells were detached from 10 cm dishes by brief trypsinization, washed once with Hank's balanced salt solution (HBSS) and resuspended in 100 μl (HBSS) on ice. PFO was added to cells to a final concentration of 100 nM and maintained on ice for 5 min. The reaction mix was supplemented with an ATP regenerating mix, 10μM HA-Ubvme or TAMRA-Ubvme and protease inhibitor cocktail, and transferred to 37°C for 20 min. The reaction was terminated with lysis buffer. TAMRA-Ubvme reactive DUBs were resolved by SDS-PAGE and visualized by fluorescence scanning, whereas HA-Ubvme labeled DUBs were first isolated on anti-HA beads, resolved by SDS-PAGE and visualized by silver staining.

Immunoprecipitation and mass spectrometry

Large-scale immunoprecipitations were performed on conjugated HA-beads (for ubiquitylated substrates) and streptavidin beads (for BioID). Entire lanes were sliced into 2 mm sections, and were further processed in 50% water/methanol. Samples were trypsinized and subjected to a Lumos Orbitrap mass spectrometer for identification of candidates. MS/MS spectra were analyzed using Sequest algorithm. The target sequences comprised the human protein repository of the Uniprot database and protein sequences corresponding to the Influenza A PR8, WSN and H1N1 pandemic strains. Decoy sequences were obtained upon reversing the orientation of target sequences. Allowed criteria for searches required trypsin cleavage (two missed cleavages allowed), peptide mass tolerance of 20 p.p.m., variable oxidation of methionine residues, and static carbamylation modification of cysteine residues. Peptide-spectrum matches were determined with estimated false discovery rate of 1%. Spectral counts for each condition were combined at a protein level and normalized by protein length to infer protein abundances and intensities in each case. Identified hits were further categorized into different biological pathways using Ingenuity Pathway Analysis software.

Isolation of OTUB1 partners in mock and virus infected cells

BioID assay

~10^6 A549 cells expressing BirA-OTUB1 were cultured in media supplemented with 1μg/ml doxycycline and 50μM biotin. Cells were lysed in 1 mL lysis buffer (50 mM Tris, pH 7.5, 150 mM NaCl, 5mM EDTA, 1 mM DTT, 0.5% TX-100 and 1X complete protease inhibitor cocktail). Lysates were incubated with 500 μl of Neutravidin beads with end-over-end rotation for 1 hour at 4°C. Bound material was washed with buffer containing 0.5% TX-100 and eluted in 50 μl of Laemmli buffer saturated with biotin. 10% of the sample was reserved for western blot analyses. Samples reserved for analyses by mass spectroscopy were washed with 50 mM NH_4HCO_3 before subjecting to protease digestion.

Quanti-blue SEAP Phosphatase assay

QUANTI-blue Gold is a two-component kit which contains: - QB reagent and – QB buffer, provided by Invivogen (HK). A standard protocol according to manufacturer's instructions was followed. The following protocol refers to the use of 96-well plates. 180 μL of QUANTI-Blue Solution was dispensed per well into a flat-bottom 96-well plate. 20 μL of sample (supernatant of SEAP-expressing cells) or negative control (cell culture medium) were added and incubated at 37°C for 15 min to 6 h. Optical density (OD) at 620nm was measured using a microplate reader.

Quanti-luc luciferase assay

QUANTI-Luc Gold is a two-component reporter kit which contains: - QUANTI-Luc Plus and - QLC Stabilizer, provided by Invivogen (HK). A standard protocol according to manufacturer's instructions was followed. Quanta-Luc pouches were dissolved in sterile water together with QLC stabilizer. 20 μl of cell supernatant was added to a white opaque 96-well plate. 50 μl of QUANTI-Luc Gold assay solution was added to each well. The measurement was carried out immediately using a luminometer.

Transient transfections and lentiviral transductions

Cells were transfected using either Fugene6 (Roche Diagnostics), TransIT or lipofectamine according to the manufacturer's instructions. For generation of lentiviral particles, 293T cells were seeded at a density of 4×10^6 cells/dish (10 cm dishes) 24h before transfection (in 12 mL of DMEM 10% FBS, 1% P/S, 1% HEPES). Transfection was carried out with TransIT reagent, following the manufacturer's instructions. Plasmids VSV-G, PLP1 (GAG/POL), PLP2 and plenti vector (plasmid of interest) were co-transfected with TransIT reagent in Opti-MEM. 24h after transfection, the supernatant was removed with a syringe, filtered on 0.22μm and stored overnight at −80°C. Virus particles collected from supernatants were concentrated by ultracentrifugation (28000 rpm, 4°C). Pellets were resuspended in 100 μl of PBS and left at 4°C for 1h to resuspend the virus. A549 cells were seeded in 10 cm dish with a density of 4×10^6 cells/dish before lentiviral transduction. Transduction was performed using 30 μl of virus/dish (with dropwise distribution). 2 days after, the medium was changed and supplemented with 5 μg/ml of blasticidin. Medium was replaced every three days and selection pressure was kept for two weeks, followed by single clonal expansions, which were verified with western blots for expression of desired protein.

Pulse-chase analysis of OTUB1 turnover

Pulse chase experiments were performed as previously described (Sanyal et al., 2013; Zhang et al., 2018a). Briefly, ~1×10^7 cells, either mock or IAV-infected were detached by trypsinization and starved for 30 min in methionine/cysteine free DMEM at 37°C prior to pulse labeling. Cells were labeled for 10 min at 37°C with 10mCi/ml [^{35}S]methionine/cysteine (expressed protein mix; PerkinElmer) and chased for indicated time intervals. At appropriate time points, aliquots were withdrawn and the reaction was stopped with cold PBS. Cell pellets were lysed in Tris buffer containing TX-100 and pre-cleared with agarose beads for 1 hour at 4°C. Immunoprecipitations were performed for 3h at 4°C with gentle agitation. Samples were eluted by boiling in reducing sample buffer, subjected to SDS-PAGE and visualized by autoradiography.

Generation of knock-out and knock-down cells

CRISPR/Cas9 mediated deletion of OTUB1

Potential target sequence for CRISPR interference were found using the rules outlined elsewhere (Mali et al., 2013). Transfection of recombinant plasmid into A549/ A549^{dual}/ 293T cells was carried out using Trans-IT. After 24 hours, cells were subjected to puromycin selection at a concentration of 3 μg/ml for A549 and 4 μg /ml for 293T. After 3 days, medium was replaced with that without puromycin and selected cells were allowed to grow for 1-2 weeks depending on the number of surviving cells. Deletion efficiency was checked in the mixed populations. For clonal expansion, selected cells were seeded in a 10 cm dish at a low density of 20 cells/dish. Pyrex® 8mm cloning cylinders were used to demarcate single colonies and silicone grease was used to create an isolated well. Trypsinized colonies from isolated cylinders were grown in 12 well-plates and verified at passages 1, 3 and 10 for complete deletion of OTUB1.

In vitro reconstitution of IRF3 dimerization

Biochemical assays for IRF3 activation with cytosolic extracts and mitochondrial preparations were as described previously (Zeng et al., 2010). Briefly, hypotonic buffer [10 mM Tris-HCl (pH 7.5), 10 mM KCl, 1.5 mM $MgCl_2$, 0.5 mM EGTA, and protease inhibitor cocktail] was used to prepare cytosol fractions, and isotonic buffer (hypotonic buffer plus 0.25 M D-Mannitol) was used to prepare mitochondrial membranes. Cells were homogenized in appropriate buffers, and centrifuged at 600 g for 5 minutes to pellet nuclei. Post-nuclear supernatants were further centrifuged at 10,500 x g for 10 minutes to collect mitochondrial membranes in the pellet fraction. Supernatants were subjected to centrifugation at 100,000 g, to separate cytosol fractions from microsomes. Pelleted mitochondrial membranes were washed once with isotonic buffer. For IRF3 pathway activation by RIG-I, the reaction mixture contained 1 mg/ml mitochondrial prep, 3 mg/ml cytosol fractions (from OTUB1-deficient cells expressing OTUB1 variants), 1xMgATP buffer [20 mM HEPES-KOH (pH7.4), 2 mM ATP, 5 mM $MgCl_2$], and [^{35}S]IRF3. After incubation at 30°C for 2 hours, samples were centrifuged at 20,000 g for 5 minutes and supernatants were subjected to native

PAGE to visualize IRF3 dimerization by autoradiography using PhosphorImager (GE Healthcare). ImageQuant was used to quantify signal intensity.

Glycerol gradient analyses

500 μL lysates from mock or infected cells was loaded onto a 3.8 mL glycerol gradient (10%–40% (w/v)) prepared in 1% (w/v) NP-40, 100 mM NaCl, 20 mM HEPES-NaOH pH 7.4. Sedimentation standards (ovalbumin (3.6S), BSA (4.2S), β-amylase (8.9S) and catalase (11.4S)) were analyzed in a parallel gradient. The gradients were centrifuged in a Beckman MLS 50 rotor at 35,000 rpm (~165,000 g_{av}) for 20 h at 4°C and fractions (300 μl) were collected from the top. The fractions collected were desalted on Bio-Gel P6 spin columns to remove glycerol, resolved by SDS-PAGE and immunoblotted to visualize separation of RIG-I and OTUB1.

Immunofluorescence assays

For fluorescence microscopy, A549 cells were seeded the day before the experiment, on slides pre-coated with Poly-L- Lysine (sigma). Seeding density used was 0.3 X 10^6 per well (in 12 well plates). Cells underwent infection with IAV or IFN type I treatment. Time points were collected by washing the slides twice with PBS, followed by fixation with 4% formaldehyde for 20 minutes and incubation in PBS at 4°C. PBS with 0.05% Triton as permeabilization agent was used for 5 minutes followed by two washes with PBS alone. The slides were blocked with either PBS + 4% FBS or PBS + 4% NGS, for 30min −1 hour at room temperature. Primary antibodies at their appropriate dilution in PBS was added and incubated for 2 hours at room temperature followed by washing twice with PBS. Secondary antibodies diluted in PBS was dispensed and incubated for 1 hour at room temperature. After two washes with PBS, the slides were stained with freshly diluted DAPI staining (sigma) for 2 minutes and rinsed twice with PBS. Slides were dried and placed on glass slides overlaid with mounting buffer and kept overnight at 4°C before visualizing with confocal microscopy.

QUANTIFICATION AND STATISTICAL ANALYSIS

Results generated for protein expression profiles and autoradiograms were analyzed by densitometry on ImageJ, from independent biological replicates (where $n \geq 3$), each measured in technical duplicates or triplicates. Results have been presented as means ± standard deviation (SD) for the specified number of experiments as described in the corresponding figure legends.

For image analyses of colocalization, Pearson's correlation coefficients were calculated. For RT-qPCR, fold changes in mRNA expression were determined using the ΔΔCt method relative to the values in control samples as indicated in figure legends, after normalization to housekeeping genes. Results obtained from luminescence, absorbance, RT-qPCR and plaque assays are presented as mean ± S.D, unless stated otherwise. Comparisons between two populations of data (e.g control and sample) were made using the Student's unpaired t test with a confidence limit for significance set at ≤ 0.05. For multi sample comparisons, two-way ANOVA was performed. All data generated were assumed to follow normal distribution and homogeneity of variance based on Q-Q plots and Levene's test. Statistical analyses were performed in GraphPad PRISM 8.0. and Bioconductor package on RStudio. Pathway enrichment of hits from BioID assay was performed using Ingenuity Pathway Analysis software.

DATA AND CODE AVAILABILITY

The published article includes all the datasets generated or analyzed during this study, except the OTUB1-BioID interaction dataset which is being used for a related manuscript under preparation, but is available from the corresponding author upon request.

Cell Reports, Volume *30*

Supplemental Information

OTUB1 Is a Key Regulator of RIG-I-Dependent Immune Signaling and Is Targeted for Proteasomal Degradation by Influenza A NS1

Akhee Sabiha Jahan, Elise Biquand, Raquel Muñoz-Moreno, Agathe Le Quang, Chris Ka-Pun Mok, Ho Him Wong, Qi Wen Teo, Sophie A. Valkenburg, Alex W.H. Chin, Leo Lit Man Poon, Artejan te Velthuis, Adolfo García-Sastre, Caroline Demeret, and Sumana Sanyal

Accession no	Protein name	Mol mass (kDa)	Unique peptides Mock	H1N1	Mowse score	No of MS/MS queries	Seq coverage
Q96FW1	Ubiquitin thioesterase protein OTUB1	37	5	21	901	30	52
Q9UHP3	Ubiquitin carboxyl-terminal hydrolase 25	122	9	14	511	22	37
Q96RU2	Ubiquitin carboxyl-terminal hydrolase 28	122	6	14	285	5	28
Q9Y614	Ubiquitin carboxyl-terminal hydrolase 3	59	12	22	140	8	15
Q92560	Ubiquitin carboxyl-terminal hydrolase BAP1	80	10	16	163	20	9
Q13107	Ubiquitin carboxyl-terminal hydrolase 4	108	28	8	57	4	12
Q9Y5K5	Ubiquitin carboxyl-terminal hydrolase isozyme L5	38	13	31	177	5	10
P15374	Ubiquitin carboxyl-terminal hydrolase isozyme L3	26	11	31	213	5	8
Q96G74	OTU domain containing protein 5	61	24	7	154	16	11
Q7L8S5	OTU domain containing protein 6A	33	11	20	284	11	7
Q9NQC7	Ubiquitin carboxyl-terminal hydrolase CYLD	107	12	34	41	4	5
P21580	Tumor necrosis factor alpha-induced protein 3	90	6	18	58	2	6
Q96DC9	Ubiquitin thioesterase OTUB2	27	7	11	44	1	8
Q9Y4E8	Ubiquitin carboxyl terminal hydrolase 15	112	10	19	31	3	10

Table S1: Identification of deubiquitylases by HA-Ubvme in primary lung epithelial cells, either mock or H1N1 (pdm) infected.
(Related to Figure 1)

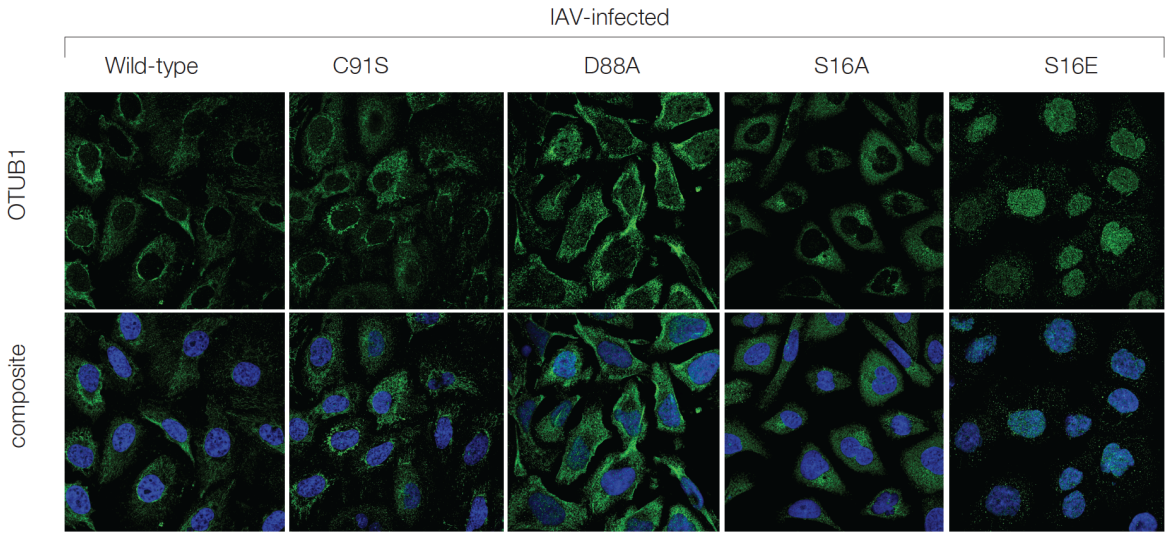

Figure S1: Subcellular distribution of OTUB1 mutant variants in IAV-infected cells (Related to Figure 3)

OTUB1$^{-/-}$ A549 cells expressing the different variants of OTUB1 were generated by lentiviral transductions. C91S; catalytic mutant, D88A; deficient in binding to and forming the E2-repressive complex, S16A; phosphorylation deficient and expected to be enriched in the cytosol, S16E; phosphomimetic and expected to be enriched in the nucleus. Subcellular distribution of the panel of OTUB1 mutants were visualised by confocal imaging in IAV (H1N1 pdm) infected A549 cells expressing the OTUB1 variants. Wild-type, C91S and S16A displayed a similar distribution – predominantly present in the cytosolic and mitochondrial compartments. D88A displayed a lack of distribution in the mitochondrial membranes whereas S16E remained confined to the nucleus upon IAV infection.

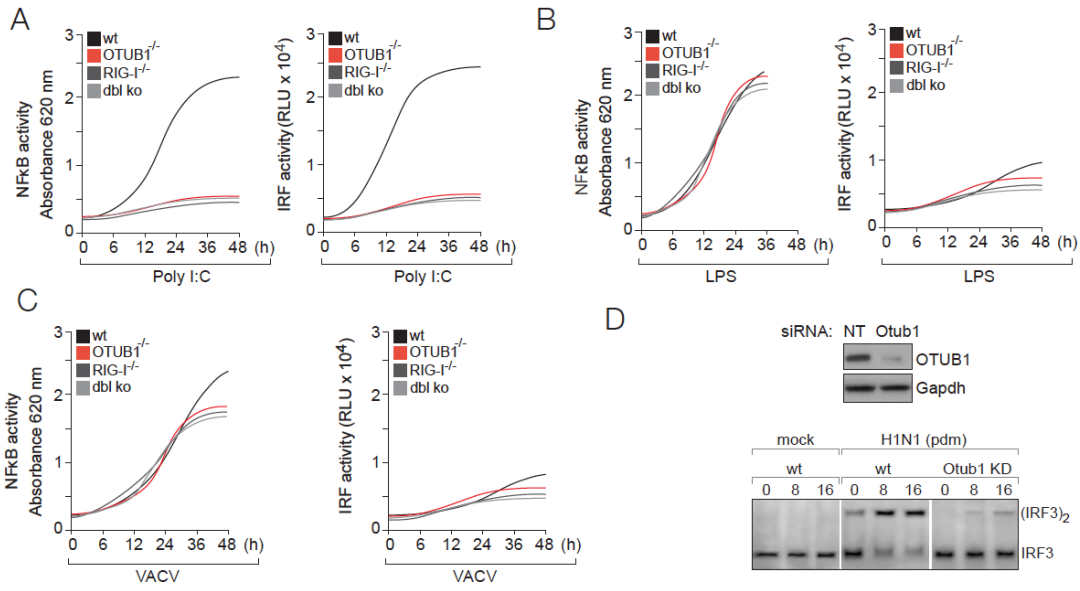

Figure S2: NFκB and IRF3 activities in Poly I:C and LPS treated cells (Related to Figure 4)

OTUB1 deletion was generated through CRISPR/Cas9 in A549 cells expressing reporters for NFκB and IRF activities measured via secreted alkaline phosphatase and luciferase respectively. OTUB1$^{-/-}$ cells were generated either in a wild-type background or those harboring a deletion of RIG-I to create a double knockout of OTUB1 and RIG-I. **(A)** The wild-type, OTUB1$^{-/-}$, RIG-I$^{-/-}$, and the double knock-out cells were treated with Poly I:C to stimulate the RIG-I pathway. **(B)** LPS-treated samples were monitored as control. OTUB1$^{-/-}$ cells displayed attenuated NFκB and IRF activities, equivalent to that of RIG-I$^{-/-}$ and the double knock-out cells, when compared to the wild-type cells, when treated with poly I:C. On the other hand, activation of NFκB in LPS treated cells remained insensitive to deletions in OTUB1 or RIG-I or the combined deletion of the two. Since LPS does not trigger IRF activity, it remained at basal levels in all cells, upon LPS treatment. **(C)** NFκB and IRF3 activities in VACV-infected cells, infected at MOI 1.0 for indicated time intervals, and measured as described in Figure 4. **(D)** Primary lung epithelial cells were treated with non-targeting (NT) scrambled siRNA and that against OTUB1. Depletion of OTUB1 was tested by immunoblotting (*upper panel*). Wild-type and OTUB1-depleted cells were mock-treated and infected with H1N1 (pdm) at MOI 1 for indicated time intervals. Lysates prepared were tested for IRF3 dimerisation using native gel electrophoresis (*lower panel*).

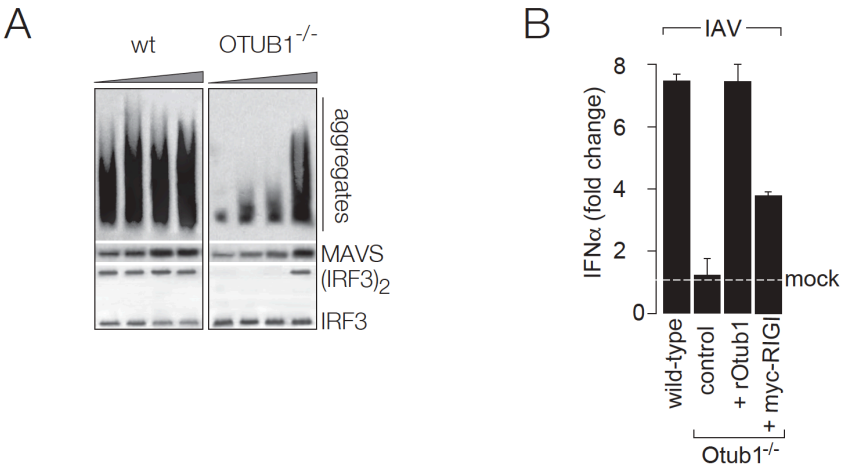

Figure S3: OTUB1 does not affect downstream of MAVS-dependent signaling (Related to Figure 5)

(A) Lysates were generated from wild-type or OTUB1$^{-/-}$ HEK293T transfected with increasing plasmid concentrations of MAVS (5, 10, 50 and 100 µg/ml) and treated with poly I:C. Lysates were resolved either by (i) semi-denaturing agarose gels (SDD-AGE) to visualise MAVS oligomerisation in wild-type and OTUB1$^{-/-}$ cells (upper panel), or (ii) by denaturing SDS-PAGE to detect MAVS expression (*middle panel*), or (iii) by native-PAGE to measure IRF3 dimerisation (*lower panel*). **(B)** Interferon production was measured from IAV-infected (H1N1 pdm, MOI 1) wild-type and OTUB1$^{-/-}$ A549 cells alongside cells reconstituted with either wild-type OTUB1 (rOTUB1), or myc-RIG-I in the OTUB1$^{-/-}$ background. Supernatants were collected at 24 hours post infection and secreted IFNα was measured either by ELISA, or FACS using a bead based assay for cytokine detection. Error bars represent mean±s.d from atleast three independent experiments.

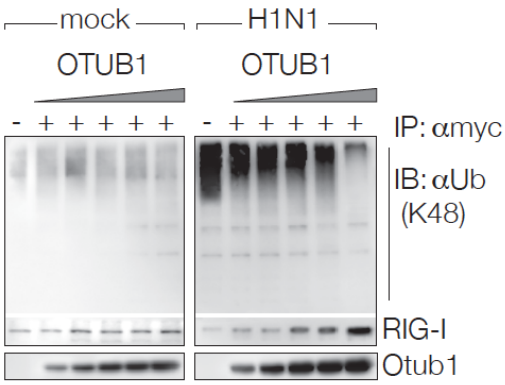

Figure S4: OTUB1 regulates ubiquitylation of RIG-I in H1N1-infected cells (Related to Figure 6).

OTUB1$^{-/-}$ HEK293T cells were co-transfected with wt ubiquitin, myc-RIG-I and increasing concentrations of wild-type OTUB1. All samples were either mock-treated or infected with H1N1 (pdm) strain (MOI 1, 12 hours). For all the samples, RIG-I was immunoprecipitated on anti-myc and associated polyubiquitin chains were detect by immunoblotting with anti-Ub (*upper panel*). Expression levels of OTUB1 were measured in the corresponding lysates (*lower panel*).

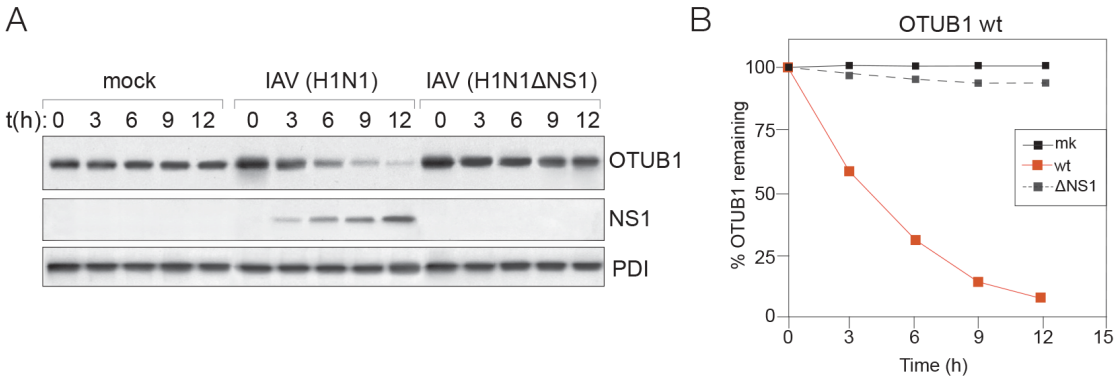

Figure S5: Influenza NS1 triggers proteasomal degradation of OTUB1 (Related to Figure 7).

(A) Pulse-chase analyses were performed with OTUB1$^{-/-}$ cells expressing WT OTUB1, and infected with either H1N1 (pdm) (WT) or ΔNS1. Infected cells were pulsed with [^{35}S]cysteine/methionine and chased for indicated time intervals. At each timepoint OTUB1 was immunoprecipitated and detected by autoradiography. NS1 was immunoprecipitated from the same samples to measuring expression at the indicated time intervals. PDI expression was measured as loading control. **(B)** Amount of OTUB1 remaining was calculated using densitometry as a percentage of total at the 0 time point, normalised to 100%. Images are representative of atleast three independent experiments.